

C O N T E N T S

SCHOOL OF ENGINEERING

Technical Papers

Characterization of the Membrane Topology and Physical Interaction of Human Dolichol-Phosphate-Glucose Synthase
..... Tetsuo TAKAHASHI, Naoto YAMADA and Riki OSHIRO..... 1

New Concept of Accident Tolerant Fuel Assembly Composed of SiC Block for KAMADO-BWR
..... Tetsuo MATSUMURA and Takanori KAMEYAMA..... 7

Generation of Ammonium Ions in Water by Atmospheric-pressure Argon Plasma Jet Irradiation at Room Temperature
..... Hiroshi KUWAHATA and Ikko MIKAMI.....15

Basic Study on Hybrid Systems to Improve the Vehicle Performance of a Small Race Car
(Investigation of Gear Ratios for Hybrid Systems Using Lap Time Simulation)
..... Ikkei KOBAYASHI, Kazuki OGAWA, Daigo UCHINO, Keigo IKEDA,
Taro KATO, Ayato ENDO, Takayoshi NARITA, Hideaki KATO and Hiroyuki MORIYAMA.....23

Numerical Analysis of the Propagation of Detonation Wave Plunging Entry of a Combustible Premixed Jet Train
..... Faming WANG, Toshiharu MIZUKAKI and Shingo MATSUYAMA.....31

Characterization of the Membrane Topology and Physical Interaction of Human Dolichol-Phosphate-Glucose Synthase

by

Tetsuo TAKAHASHI*¹, Naoto YAMADA*² and Riki OSHIRO*³

(Received on Mar. 31, 2022 and accepted on May 27, 2022)

Abstract

Human dolichol-phosphate-glucose synthase (hDPGS) is resident on the rough endoplasmic reticulum (rER) membrane and provides three glucosyltransferases involved in the late assembly stage of dolichol-linked oligosaccharides (DLOs), which are precursors of *N*-glycan, with dolichol-phosphate-glucose (DPG) as donor substrate. In this study, we analyzed the membrane topology of hDPGS using the yeast split-ubiquitin system (YSUS). The obtained data demonstrated that hDPGS includes two transmembrane domains (TMDs) and orientates both *N*- and *C*- termini toward the cytosolic side of the rER membrane. In addition, using the YSUS, we demonstrated that hDPGS physically interacts with human *N*-acetylglucosamine-1-phosphate transferase (hGPT), hDPM2 and hDPM3 transmembrane subunits of human dolichol-phosphate-mannose (DPM) synthase (hDPMS), human dolichol kinase (hDK) and human dolichol pyrophosphate phosphatase (hDPP). These results strongly suggest that hDPGS cooperates with other dolichol-phosphate (Dol-P)-related enzymes in the biosynthetic pathway of DLO.

Keywords: Dolichol-phosphate glucose synthase, Dolichol-linked oligosaccharide, Split-ubiquitin system, Membrane topology, Physical interaction

1. Introduction

N-glycosylation is one of the important events for the maintenance of both structure and function of many glycoproteins in higher eukaryotes. The *N*-glycans on glycoproteins are primarily derived from the dolichol-linked oligosaccharides (DLOs), which are biosynthesized on the rough endoplasmic reticulum (rER) membrane¹. As shown in Fig. 1, the assembly process of DLOs is further divided into three stages: first, early assembly of up to Man₅GlcNAc₂-PP-dolichol (Dol) on the cytoplasmic side by UDP-GlcNAc or GDP-Man dependent glucosyltransferases; second, translocation of Man₅GlcNAc₂-PP-Dol into the luminal side by a putative flippase; and finally, late assembly of full-sized DLO (Glc₃Man₉GlcNAc₂-PP-Dol) by three dolichol-phosphate-mannose (DPM)-dependent mannosyltransferases (hAlg 3, hAlg9 and hAlg12) and three dolichol-phosphate-glucose (DPG)-dependent glucosyltransferases (hAlg6, hAlg8 and hAlg10)²⁻⁵. These highly ordered steps are well conserved all through eukaryotes.

The DPG synthase (DPGS) catalyzes the transfer reaction of glucose (Glc) from UDP-Glc to Dol-P, forming DPG, which is utilized by hAlg6, hAlg8 and hAlg10 (red arrow in Fig. 1

*1 Associate Professor, Department of Applied Biochemistry

*2 Undergraduate Student, Department of Applied Biochemistry

*3 Graduate Student, Course of Applied Science and Chemistry

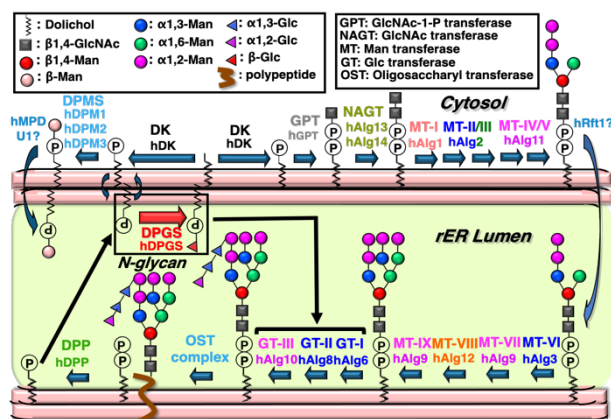


Fig. 1 Assembly of dolichol-linked oligosaccharides (DLOs) and site of action regarding the human dolichol-phosphate-glucose synthase (hDPGS). DK and DPP indicate dolichol kinase and dolichol pyrophosphatase, respectively.

and Ref. 6). The gene encoding the DPGS was firstly identified in the budding yeast as the *ALG5* gene by complementation assay of the yeast *alg5* mutation, which causes accumulation of Man₉GlcNAc₂-PP-dolichol, an intermediate DLO, at non-permissive temperature⁷. Later on, by searching EST databases and using low-stringency PCR amplification to screen a human T-lymphocyte cDNA library, a human *DPGS* cDNA encoding the ortholog of *S. cerevisiae* *ALG5* was isolated⁸. The human *DPGS* gene encodes human

Table I The PCR primers used in this study. Additional sequences containing a *Sfi* I- cleavage site are shown in lowercase letters.

Primer name	Nucleotide sequence	Purpose
hA5BPfw	5'-tgtaatggccattacggccATGGCTCCGCTTCTGTTGCAGCTGG-3'	PCR cloning of the <i>hDPGS</i> into pBT-N, pBT-C, pPR-N and pRR-C
hA5BPrv	5'-gcctttggccgagggcgcccttATTCATTTTCCGAGTTTGTCTCAAGCCTC-3'	PCR cloning of the <i>hDPGS</i> into pBT-N, pBT-C, pPR-N and pPR-C
hA5HR1rv	5'-gcctttggccgagggcgccTCTTCATGTCGATGGAGTGCTGG-3'	PCR cloning of the <i>hDPGS</i> from <i>N</i> -terminus to HR1 into pBT-C
hA5LR2rv	5'-gcctttggccgagggcgccGTACGGAAGTAAGAACGCTGAG-3'	PCR cloning of the <i>hDPGS</i> from <i>N</i> -terminus to LR2 into pBT-C
hA5HR2rv	5'-gcctttggccgagggcgccTCTCGAGTAAATAATTTGAACCCACA-3'	PCR cloning of the <i>hDPGS</i> from <i>N</i> -terminus to HR2 into pBT-C
hA5LR3rv	5'-gcctttggccgagggcgccTTAGAACCTTCAATTTCTGTCCAG-3'	PCR cloning of the <i>hDPGS</i> from <i>N</i> -terminus to LR3 into pBT-C
hA5HR3rv	5'-gcctttggccgagggcgccGTCAAATATCGAAGTCGTATAAAAAG-3'	PCR cloning of the <i>hDPGS</i> from <i>N</i> -terminus to HR3 into pBT-C

DPGS (hDPGS) protein, which consists of 324 amino acids and shows 37% identity to the yeast Alg5p. Expression of the human *DPGS* cDNA could partially complement the *S. cerevisiae alg5* deficiency⁸.

Although membrane topology and physical interaction of the yeast Alg5p have been characterized^{9,10}, those of hDPGS remained to be analyzed in detail. Therefore, in this study, we first investigated the membrane topology of hDPGS using the yeast split-ubiquitin system (YSUS)⁹⁻¹³, a yeast two-hybrid system that can specifically detect the physical interaction between two membrane proteins¹⁴⁻¹⁶. Moreover, we also characterized the physical interactions of hDPGS with other enzymes involved in the DLO assembly using the YSUS.

2. Experimental Methods

2.1 Prediction of the membrane topology of hDPGS

In order to predict the membrane topology of hDPGS protein, a WWW algorithms servers, TOPCONS¹⁷ (<https://topcons.cbr.su.se>) was used. On its WEB site, the amino acid sequence of hDPGS protein consisting of 324 residues was registered and surveyed regarding its transmembrane domain (TMD) and membrane topology.

2.2 Construction of recombinant plasmids for the YSUS

The coding region of *hDPGS* gene was amplified from the human cDNA pools derived from the human brain by standard PCR method¹⁸ using specific primers listed in Table 1. It was then digested with *Sfi* I, purified and ligated to the pBT-N or pBT-C plasmid vector for expression of hDPGS bait protein which has Cub (*C*-terminal half of *ubiquitin* protein) tag prepared in the YSUS, at the *N*- or *C*- terminus, respectively. Preparation of each recombinant plasmid was conducted by standard cloning method¹⁹ with the *Escherichia coli* JM109 strain. The constructs for expression of hDPGS prey protein were also prepared by the same procedure, except usage of the pPR-N and pPR-C plasmid vectors instead of pBT-N and pBT-C.

In order to analyze membrane topology of hDPGS, five pBT-C vector-based constructs for expression of truncated versions of hDPGS bait protein in yeast cell, pBT-C-hDPGS/HR1, pBT-C-hDPGS/LR2, pBT-C-hDPGS/HR2, pBT-C-hDPGS/LR3 and pBT-C-hDPGS/HR3, were prepared via

PCR cloning described above.

In order to analyze the physical interactions of the hDPGS with thirteen other enzymes involved in DLO assembly (shown in Fig. 1), the prey constructs²⁰ for their expression were also prepared via PCR cloning described above.

2.3 Assays for the membrane topology of the hDPGS

The bait constructs, pBT-N-hDPGS, pBT-C-hDPGS and four pBT-C-hDPGS LR series were used for co-transformation of the *Saccharomyces cerevisiae* NMY51 strain, together with the positive or negative control prey construct, pAI-Alg5 or pDL-Alg5. The transformation of the yeast cells was carried out by the standard method²¹. The co-transformants obtained on the synthetic dextrose (SD) medium lacking leucine and tryptophan (SD-LW) were then subject to the growth examination on the SD medium lacking leucine, tryptophan and histidine (SD-LWH) and SD medium lacking leucine, tryptophan, histidine and adenine (SD-LWHA) according to the manual supplied by Dualsystems Biotech (www.dualsystems.com).

2.4 Assays for the physical interaction of hDPGS

The bait construct, pBT-N-hDPGS or pBT-C-hDPGS was combined with any prey construct of thirteen enzymes involved in DLO assembly (shown in Fig. 1), and then they were used for co-transformation of the yeast NMY51 strain. After the co-transformation, the co-transformants grown on SD-LW medium were subject to growth examination with SD-LWH and SD-LWHA media, according to the same procedure as described above.

3. Results and Discussion

3.1 The membrane topology of hDPGS

hDPGS protein is composed of 324 amino acid residues. First, we started from predicting the membrane topology of hDPGS protein with TOPCONS algorithms, a server freely available on WEB sites. As shown in Fig. 2, TOPCONS algorithm consequently predicted four loop regions (LRs 1 to 4) and three hydrophobic regions (HRs 1 to 3), corresponding to TMDs, in hDPGS protein (Fig. 2, lower panel). It also predicted that its *N*- and *C*- termini would be orientated toward luminal and cytoplasmic sides of the rER membrane,

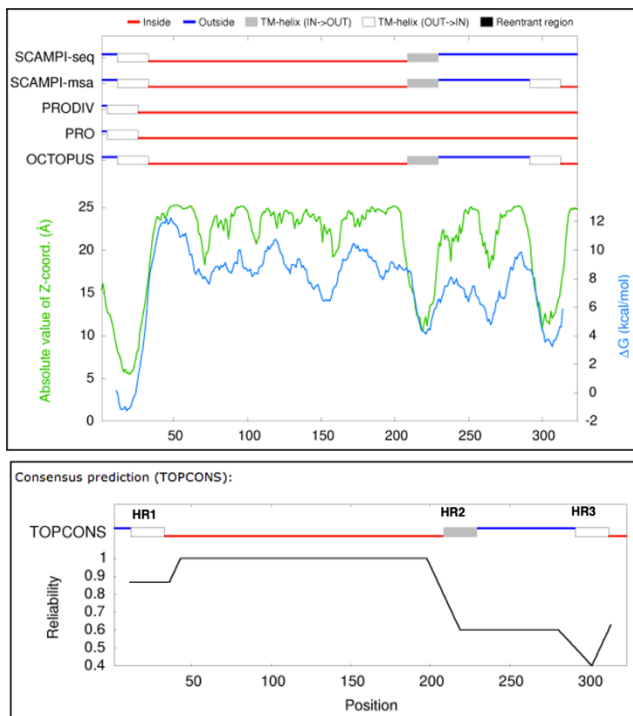


Fig. 2 Prediction of the membrane topology of hDPGS by TOPCONS algorithm server (<http://topcons.cbr.su.se/>). Five independent algorithms were firstly used for prediction of membrane topology of hDPGS in the upper panel, and their consensus prediction was subsequently represented in the lower panel. The three hydrophobic regions (HR1, HR2 and HR3) were detected in hDPGS as transmembrane domains (TMDs).

respectively (Fig. 2, lower panel). These predictions partly agreed with the membrane topological model of the yeast Alg5p protein previously obtained by the YSUS analysis^{9,10}.

In order to confirm the predictions, we also applied the YSUS to our analysis of hDPGS. The negative and positive control prey constructs (pDL-Alg5 and pAI-Alg5, respectively) prepared in the YSUS are designed to express Nub (*N*-terminal half of ubiquitin protein) tag terminally fused to the Alg5 protein in cytoplasmic side of the rER, and readily available to ascertain whether the terminal Cub tag of the bait protein expressed on the rER membrane is located in the cytoplasm or lumen^{20,22,23}. Therefore, we prepared two bait constructs, pBT-N-hDPGS and pBT-C-hDPGS, which express a full-length hDPGS protein with *N*- and *C*-terminal Cub tags, respectively. We also prepared four additional bait constructs, pBT-C-hDPGS/HR1, pBT-C-hDPGS/LR2, pBT-C-hDPGS/HR2 and pBT-C-hDPGS/LR3, each of which expresses a truncated version of hDPGS, whose *C*-terminal Cub tag is respectively fused to HR1, LR2, HR2 or LR3 of hDPGS (Fig. 3, panel B). Each bait construct was combined with the pDL-Alg5 or pAI-Alg5 control prey, and then they were used for co-transformation of the yeast NMY51 cells.

In growth examination of resultant co-transformants grown on SD-LW plates, co-transformants of the pBT-N-hDPGS or pBT-C-hDPGS bait with the pAI-Alg5 positive control prey have well grown on SD-LWH and SD-LWHA plates (upper red frame in Fig. 3A), indicating that the terminal

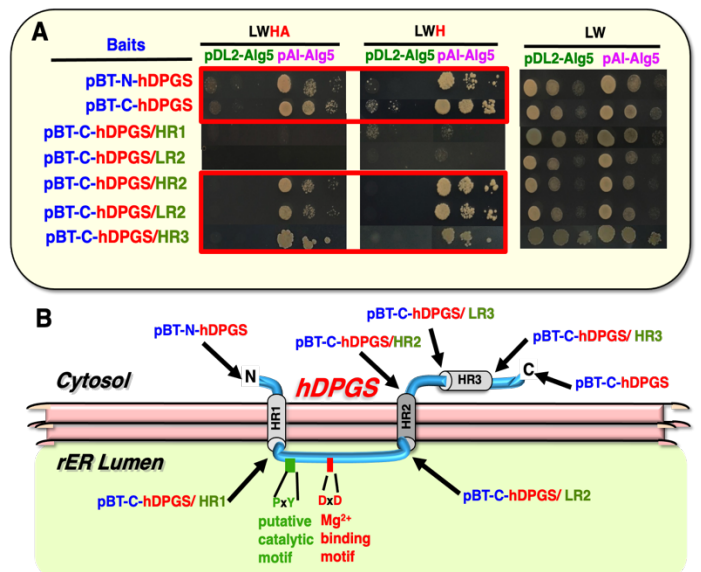


Fig. 3 (A) Growth examination of co-transformants with hDPGS baits / control prey constructs. After the selection of colonies derived from the co-transformants on the SD-LW medium, their suspensions were diluted with sterilized water and adjusted to the OD₆₀₀ values of 1.0, 0.1 and 0.01 (from left to right). These diluents were orderly spotted on the SD-LWH and SD-LWHA media for reporter detection, and SD-LW media for growth control, and then incubated at 30 °C for 2~4 days. (B) The model of membrane topology of hDPGS based on the YSUS analyses. Each Arrow indicate position of Cub tag in hDPGS bait protein expressed with seven hDPGS bait constructs used in examination (A), where it was analyzed whether the fused Cub tags were resided in cytosol or rER lumen.

Cub tag fused to hDPGS protein specifically interacted with Nubi (normal type of Nub) tag of pAI-Alg5 located in cytoplasm. On the contrary, those with the pDL-Alg5 negative control prey exhibited no growth on both media (Fig. 3A), because NubG (mutational type of Nub) tag of pDL-Alg5 located in cytosol is not able to spontaneously interact with Cub tag located in cytosol²⁰. From these results, it was concluded that both *N*- and *C*- termini of hDPGS should be located in the cytoplasmic side of the rER membrane (Fig. 3B).

In the five kinds of co-transformants where truncated hDPGS bait protein and the pAI-Alg5 positive control prey protein are co-expressing, those with the pBT-C-hDPGS/HR2, pBT-C-hDPGS/LR3 and pBT-C-hDPGS/HR3 displayed growth activities on SD-LWH and SD-LWHA media (lower red frame in Fig. 3A), while those with the pBT-C-hDPGS/HR1 and pBT-C-hDPGS/LR2 did not (Fig. 3A).

Taken together, these observations demonstrated that *N*-terminal loop region (LR1), the third loop region (LR3) and hydrophobic region (HR3), and *C*-terminal loop region (LR4) of hDPGS are located in the cytosolic side of the rER membrane and that the second loop region (LR2) is located in the luminal side of the rER membrane (Fig. 3B). This model of the membrane topology of the hDPGS coincides with that of the yeast Alg5p previously proposed^{9,10}, although the possibility that the HR3 of the hDPGS would be a potential membrane-embedded domain cannot be excluded. As shown in Fig. 3B, the hDPGS possesses a DxD motif, which might

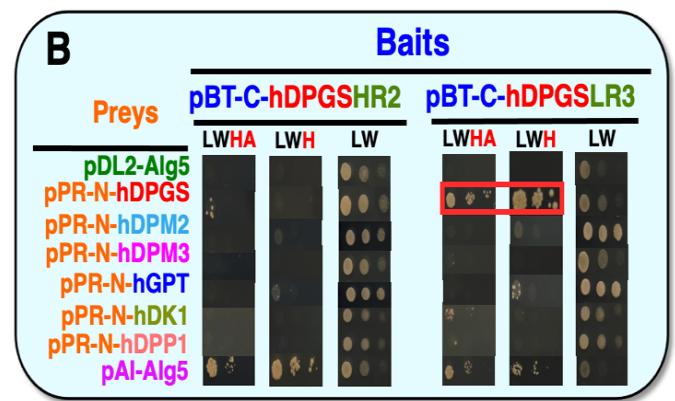
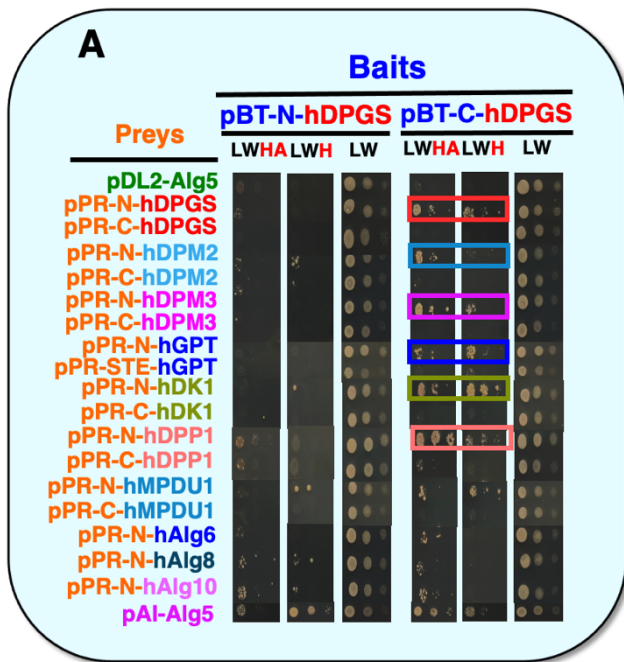


Fig. 4 (A) Growth examination of co-transformants of two full-length hDPGS baits with preys of various glycosyltransferases involved in DLO assembly. (B) Growth examination of co-transformants of two truncated hDPGS baits with preys of six glycosyltransferases, of which physical interactions with full-length hDPGS were detected in panel A. The experiments were performed according to the same procedure as described in the legend of Fig. 3.

bind the co-factor Mg^{2+} ion, and a putative catalytic motif PxY in LR2. Therefore, LR2 estimated to be located within the rER lumen should be a catalytic domain. This means that available donor substrate for the DPGS would be limited, because the donor substrate, UDP-Glc, is biosynthesized in the cytoplasm and partially transported into the rER lumen by the specific transporters²²). In addition, against UDP-Glc, the DPGS would always compete with the UDP-Glc: glycoprotein glucosyltransferase (UGGT) located within the rER. In contrast, availability of the acceptor substrate for the DPGS seems to be not relatively limited. The acceptor substrate, Dol-P, is *de novo* biosynthesized by dolichol kinase (DK) on the cytosolic side of the rER membrane and freely flipp-flopped through the rER membrane (Fig. 1). Moreover, Dol-P is also reproduced by dolichol pyrophosphatase (DPP) in the luminal side of the rER membrane (Fig. 1). As two other Dol-P dependent enzymes, the DPMS and GPT, orientate their catalytic domains toward cytoplasmic side (Fig. 1), the DPGS would not directly compete with these enzymes for Dol-P.

3.2 The physical interaction of hDPGS

In order to test whether hDPGS physically interacts with other enzymes in the same DLO assembly pathway, the bait construct, pBT-N-hDPGS or pBT-C-hDPGS, was combined with each prey construct of various enzymes which participate in DLO assembly, including hDPGS itself, and the co-transformations of NMY51 cells were conducted. The results of growth examination of co-transformants are shown in Fig. 4.

First, we successfully detected physical interactions of the hDPGS with six proteins using pBT-C-hDPGS bait construct, while we could not using pBT-N-hDPGS bait construct (colored frames in Fig. 4A). Co-transformants with pBT-C-hDPGS/pPR-N-hDPGS were able to grow on LWH and LWHA media. However, those with pBT-N-hDPGS/pPR-N-hDPGS, pBT-N-hDPGS/pPR-C-hDPGS and pBT-C-hDPGS/pPR-C-hDPGS were not (Fig. 4A).

These observations suggested that two hDPGS molecules might associate with each other in a specific manner, perhaps

in a head-to-tail manner, to form homo-dimer on the rER membrane (Fig. 5). Viability of co-transformants of pBT-C-hDPGS with pPR-N-hDPM2 or pPR-N-hDPM3 on both selective media suggested that hDPGS might closely associate with two transmembrane subunits of the human DPM synthase (hDPMs) (Fig. 4A). Otherwise, physical interactions of hDPGS with human *N*-acetylglucosamine-1-phosphate transferase (hGPT), human dolichol kinase (hDK) and human dolichol-pyrophosphatase (hDPP) were also detected (Fig. 4A). It appeared that hDPGS would not physically interact with hMPDU1, which play an essential role in usage of DPM yielded by hDPMs for luminal DPM-dependent mannosyltransferases (Ref. 23 and Fig. 1), and three DPG-dependent glucosyltransferases (Fig. 4A).

Next, we used three truncated bait constructs for the further Y2H analysis, instead of pBT-C-hDPGS. From the results shown in Fig. 3A, it has been demonstrated that the Cub tags expressed from pBT-C-hDPGS/HR2, pBT-C-hDPGS/LR3, and pBT-C-hDPGS/HR3 were orientated toward cytosolic side, while those from pBT-C-hDPGS/HR1 and pBT-C-hDPGS/LR2 bait constructs toward rER luminal side. Hence, the former bait constructs were applicable for analysis of physical interaction.

When the pBT-C-hDPGS/HR3 bait construct was used in the assay, the same pattern of the interactions observed with the pBT-C-hDPGS bait construct, represented in Fig. 4A, was again detected (data not shown). When the pBT-C-hDPGS/LR3 bait construct was used, physical interaction between two hDPGS molecules were still maintained (red frame in Fig. 4B). On the contrary, it was abolished when the pBT-C-hDPGS/HR2 bait construct was used (Fig. 4B). These observations suggest that the LR4 (C-terminal loop region) and HR3 of hDPGS would not necessary for homo-dimerization of the enzyme and that the LR3 of hDPGS of one side should be required for homo-dimerization (Fig. 5).

Physical interactions of hDPGS with hDPM2, hDPM3, hGPT, hDK and hDPP, detected using pBT-C-hDPGS or pBT-C-hDPGS/HR3 bait, completely disappeared when the pBT-C-

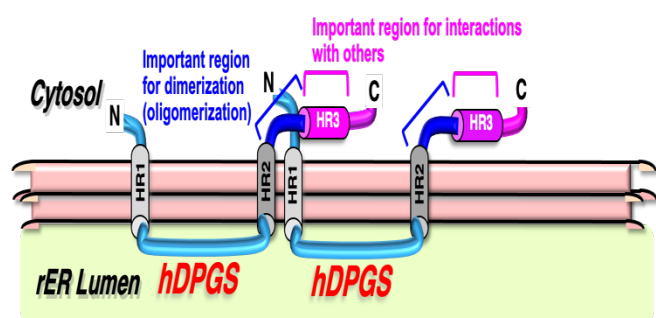


Fig. 5 The putative model of a state of hDPGS on the rER membrane speculated by the YSUS analyses in this study. The two hDPGS proteins could associate with each other in head-to-tail manner, to form homo-dimeric complex on the rER membrane via LR3.

hDPGS/LR3 bait was used (Fig. 4B), suggesting that all of them should entirely depend on the HR3 (Fig. 5). In conclusion, we propose a model for the state of hDPGS on the rER membrane, as represented in Fig. 5.

hDPGS might physically interact with hDPMS and hGPT, two enzymes which utilize Dol-P, the same acceptor substrate. Therefore, it is possible that interactions of hDPGS with them potentially occur as a result of competition. In addition, hDPGS also physically interacts with hDK and hDPP, two Dol-P-producing enzymes. Interestingly, physical interactions with hDK and hDPP have been also demonstrated for hDPMS²⁴) and hGPT²⁵), as well as hDPGS. Taken together, hDPGS, hDPMS and hGPT were estimated to assemble together around hDK and hDPP, forming into a supra-complex, possibly because they need to conduct sequential reactions on the rER membrane, where their free behavior is extremely restricted, as efficiently as possible. This possibility is additionally supported by our unpublished observation that the physical interaction between hDK and hDPP would also exist.

5. Conclusion

In order to determine the membrane topology of hDPGS involved in the assembly of DLO, the YSUS was utilized. Growth tests on the YSUS demonstrated that hDPGS protein contains at least two TMDs, with both *N*- and *C*-termini located in the cytoplasm and that its catalytic domain might be localized within the rER lumen.

Regarding the physical interactions of hDPGS, we obtained several novel informations via analyses by YSUS ; Firstly, hDPGS might homo-dimerize on the rER membrane. Secondly, hDPGS might specifically contact with two Dol-P-utilizing enzymes and two Dol-P-producing enzymes in DLO biosynthetic pathway. Thirdly, the region critical for homo-dimerization of hDPGS is clearly different from that for interactions with other enzymes.

The physical interaction between two membrane enzymes could play a role in positively or negatively altering their enzymatic activities. Our observation that hDPGS physically interacts with itself, hDK, hDPP, hDPMS and hGPT suggests that their enzymatic activities might influence each other and therefore possibility that there could exist the regulatory mechanism for Dol-P metabolism at protein level. In order to

establish the importance of this enzyme in Dol-P metabolism, further analyses are necessary to be carried out.

References

- 1) M. Aebi, *N*-linked protein glycosylation in the ER, *Biochim. Biophys. Acta* Vol.1833, pp.2430-2437 (2013).
- 2) A. D. Elbein, Inhibitors of the biosynthesis and processing of *N*-linked oligosaccharides, *CRC Crit.Rev. Biochem.* Vol.16, pp.21-49 (1984).
- 3) A. Herscovics and P. Orlean, Glycoprotein biosynthesis in yeast, *FASEB J.* Vol.7, pp.540-550 (1993).
- 4) M. A. Kukuruzinska, M. L. E. Bergh and B. J. Jackson, Protein glycosylation in yeast, *Ann. Rev. Biochem.* Vol.56, pp.915-944 (1987).
- 5) C. B. Hirschberg and M. D. Snider, Topography of glycosylation in the rough endoplasmic reticulum and Golgi apparatus, *Annu. Rev. Biochem.* Vol.56, pp.63-87 (1987).
- 6) T. Takahashi, Dolichyl-phosphate beta-glucosyltransferase (ALG5), *Handbook of glycosyltransferases and related genes*, 2nd edition, Springer, chapter 146, pp.1649-1655 (2014).
- 7) S. te Heesen, L. Lehle, A. Weissmann and M. Aebi, Isolation of the *ALG5* locus encoding the UDP-glucose: dolichyl-phosphate glucosyltransferase from *Saccharomyces cerevisiae*. *Eur. J. Biochem.* Vol.224, pp.71-79 (1994).
- 8) T. Imbach, P. Burda, P. Kuhnert, R. A. Wevers, M. Aebi, E. G. Berger and T. Hennet, A mutation in the human ortholog of the *Saccharomyces cerevisiae ALG6* gene causes carbohydrate-deficient glycoprotein syndrome type-Ic, *Proc. Natl. Acad. Sci. USA* Vol.96, pp.6982-6987 (1999).
- 9) I. Stagljar, C. Korostensky, N. Johnsson and S. te Heesen, A genetic system based on split-ubiquitin for the analysis of interactions between membrane proteins *in vivo*, *Proc. Natl. Acad. Sci. USA* Vol.95, pp.5187-592 (1998).
- 10) M. J. Massaad and A. Herscovics, Interaction of the endoplasmic reticulum alpha 1,2-mannosidase Mns1p with Rer1p using the split-ubiquitin system. *J. Cell Sci.* Vol.114, pp.4629-4635 (2001).
- 11) N. Johnsson and A. Varshavsky, Split ubiquitin as a sensor of protein interactions *in vivo*, *Proc. Natl. Acad. Sci. USA* Vol.91, No.22, pp.10340-10344 (1994).
- 12) M. Fetchko and I. Stagljar, Application of the split-ubiquitin membrane yeast two-hybrid system to investigate membrane protein interactions, *Methods* Vol.32, pp.349-362 (2004).
- 13) S. Thaminy, J. Miller and I. Stagljar, The split-ubiquitin membrane-based yeast two-hybrid system, *Methods. Mol. Biol.* Vol.261, pp.297-312 (2004).
- 14) M. Dünnwald, A. Varshavsky and N. Johnsson, Detection of transient *in vivo* interaction between substrate and transporter during protein translocation into the endoplasmic reticulum, *Mol. Biol. Cell* Vol.10, pp.329-344 (1999).
- 15) W. Scheper, S. Thaminy, S. Kais, I. Stagljar and K. Römisch, Coordination of *N*-glycosylation and protein

- translocation across the endoplasmic reticulum membrane by Sss1 protein, *J. Biol. Chem.* Vol.278, No.39, pp.37998-38003 (2003).
- 16) A. Yan and W. J. Lennarz, Studies on yeast oligosaccharyl transferase subunits using the split-ubiquitin system: Topological features and *in vivo* interactions, *Proc. Natl. Acad. Sci. USA* Vol.102, No.20, pp.7121-7126 (2005).
 - 17) K. D. Tsirigos, C. Peters, N. Shu, L. Käll and A. Elofsson, The TOPCONS web server for consensus prediction of membrane protein topology and signal peptides, *Nucleic Acids Res.* 43 (Web Server issue) W401-407 (2005).
 - 18) H. A. Erlich, PCR Technology, Stockton Press, pp.61-70 (1989).
 - 19) L. Sambrook, E. F. Fritsch and T. Maniatis, *Molecular Cloning: A Laboratory Manual*. Second edition, Cold Spring Harbor Laboratory Press, NY (1989).
 - 20) T. Takahashi and X.-D. Gao, Physical interactions among human glycosyltransferases involved in dolichol-linked oligosaccharide biosynthesis, *Trends in Glycoscience and Glycotechnology* Vol.24, pp.65-77 (2012).
 - 21) H. Ito, Y. Fukuda, K. Murata and A. Kimura, Transformation of intact yeast cells treated with alkali cations, *J. Bacteriol.* Vol.153, No.1, pp.163-168 (1983).
 - 22) M. Handford, C. Rodriguez-Furlán and A. Orellana, Nucleotide-sugar transporters: structure, function and roles *in vivo*, *Braz. J. Med. Biol. Res.* Vol.39, pp.1149-1158 (2006).
 - 23) M. Anand, J. S. Rush, S. Ray, M.-A. Doucey, J. Weik, F. E. Ware, J. Hofsteenge, C. J. Waechter and M. A. Lehrman, Requirement of the Lec35 gene for all known classes of monosaccharide-P-dolichol-dependent glycosyl-transferase reactions in mammals, *Mol. Biol. Cell* Vol.12, pp.487-501 (2001).
 - 24) T. Takahashi, N. Yamada and N. Kurimoto, Analyses on the physical interactions of the human dolichyl-phosphate mannanose synthase, *Proc. Schl. Eng. Tokai Univ., Ser. J.* Vol.57, No.1, pp.5-10 (2017).
 - 25) T. Takahashi, K. Nishimura, N. Maeda and R. Oshiro, Characterization of the membrane topology and physical interaction of the human N-acetylglucosamine-1-phosphate transferase, *Proc. Schl. Eng. Tokai Univ., Ser. E.* Vol.46, pp.1-6 (2021).

New Concept of Accident Tolerant Fuel Assembly Composed of SiC Block for KAMADO-BWR

by

Tetsuo MATSUMURA*¹ and Takanori KAMEYAMA*²

(Received on April 12, 2022 and accepted on May 27, 2022)

Abstract

We propose a new concept of accident tolerant fuel assembly composed of an SiC block for current commercial BWRs or ABWRs, which is called the "KAMADO-BWR" assembly. The KAMADO-BWR assembly is designed as one type of replacement fuel assembly for commercial BWRs or ABWRs. Conventional UO₂ fuel pellets are enclosed in many holes (fuel stacks) in the SiC block. The melting point of SiC and UO₂ is higher than 3000 K and these ceramic materials scarcely produce hydrogen with light water coolant. Most of the heat generated at the fuel pellets is significantly transferred through the SiC block, and it is removed by the two-phase flow of light water coolant inside or outside the SiC block. The thermal hydraulic and neutron reaction properties of the KAMADO-BWR assembly, such as maximum temperature, critical heat flux (CHF), infinite multiplication factor (*k-inf*) and peaking power ratio were estimated with analytical methods, and they were equivalent to those of the commercial BWR fuel assembly. It is possible to lower the maximum fuel temperature by increasing the number of fuel stacks and decreasing the power density of each fuel stack in the assembly, which can improve the safety margin. Accordingly, the KAMADO-BWR assembly is expected to be one candidate for the accident tolerant and replacement fuel assemblies for commercial BWRs or ABWRs.

Keywords: KAMADO-BWR, SiC block, Accident tolerant fuel (ATF), Critical heat flux (CHF), Replacement fuel

1. Introduction

The severe accident of the Fukushima Daiichi has shown that under such extreme conditions, nuclear fuel claddings generated hydrogen at high temperature over 1400 K by reactions with water or steam. Large amount of the generated hydrogen exploded and caused serious damage to the plant.

Recently, attention to accident tolerant fuel (ATF) is increasing, which has more resistant to fuel failure and hydrogen generation. SiC based cladding tubes, chromium coated tubes on zirconium alloy or other various ATF designs have been proposed and their related researches and developments are progressing^{1, 2)}.

We have been proposing a new concept of fuel assembly and core that is called the KAMADO (a classical hot range in Japanese), in which we make use of the solid heat transfer and multiple heat paths to coolant^{3 - 5)}. The KAMADO concept is applied to commercial BWRs, and two types of fuel assemblies are constructed as shown in Fig. 1. The fuel pellets are enclosed in many holes in an SiC block, and the generated heat at the fuel pellets is transferred through the SiC block to the two-phase flows similar to the BWR fuel assembly. The fuel pellets in Fig. 1 (a) are equivalent to the BWR 9×9 type, and (b) are equivalent to the BWR 11×11 type. These fuel

concepts can improve accident tolerance with an SiC block instead of metal claddings to prevent generating hydrogen.

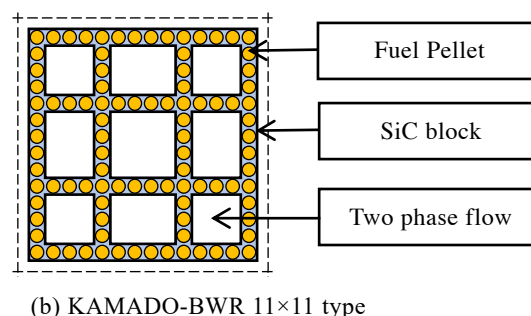
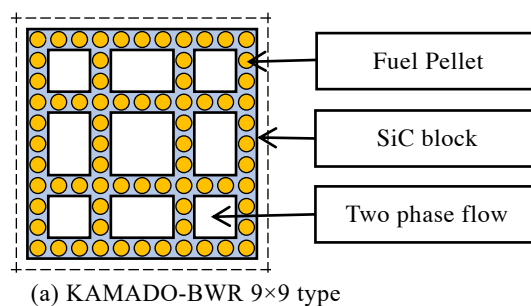


Fig. 1 KAMADO-BWR fuel assemblies.

*1 Part-time Lecturer, Department of Nuclear Engineering

*2 Professor, Global Research Institute of Nuclear Energy

In this paper, results of temperature, thermal hydraulic, mechanical and neutron reaction analyses for the KAMADO-BWR fuel assembly are described. SiC materials, fabrication methods, thermal conductivity, super-critical heat flux and severe accident cases for the fuel assemblies are also discussed.

2. Fuel temperature analyses

The specifications of the KAMADO-BWR fuel assembly are listed in Table 1. Common items of the KAMADO-BWR such as assembly outer dimensions are the same as those of the commercial BWR 9×9-B fuel assembly⁶⁾. The KAMADO-BWR fuel assembly can be used as a replacement fuel assembly for commercial BWRs or ABWRs.

Table 1 Specifications of the KAMADO-BWR fuel assembly.

Item	Value
KAMADO-BWR common	
Assembly outer dimension	139.0 mm × 139.0 mm
Assembly height	3.710 m
Assembly pitch	152.4 mm
Assembly generation power	4.31 MW
Plant pressure	7.02 MPa
Saturated temperature	560 K
Coolant mass flow	17.6 kg/s
(a) 9×9 type	
Pellet diameter	9.6 mm
Number of fuel stacks	72
Fuel pitch	12.6 mm
Uranium weight	168 kg
(b) 11×11 type	
Pellet diameter	8.2 mm
Number of fuel stacks	96
Fuel pitch	9.93 mm
Uranium weight	162 kg

Since the specifications of BWR 11×11 such as the fuel pellet diameter is not still published, the values of PWR 17×17 are used here that are closed to those of BWR 11×11.

The fuel temperature distribution was calculated with the finite element analysis system LISA⁷⁾. Assuming that the axial power peaking ratio to the average power rate was realistic value 1.4, the horizontal temperature distributions at the axial peaking position are shown in Fig. 2. Since the thermal conductivity of SiC is high (200 W/m/K), the maximum temperature on the fuel pellets center is (a) 1313 K in the BWR 9×9 type and (b) 1128 K in the BWR 11×11 type, respectively. The thermal conductivity of UO₂ fuel pellet was set to 2.54 W/m/K, which is a conservative value. The temperature of the SiC block is suppressed to 580 K close to the temperature of the two-phase flow (560 K). The heat transfer coefficient *h* from the SiC block to the two-phase flow is 94 kW/m²/K for the BWR 9×9 type or 89 kW/m²/K for the BWR 11×11 type respectively, which is calculated with the Jens-Lottes equation⁸⁾

in Eqs. (1),

$$\Delta T = \frac{0.82}{e^{63}} q_w^{\frac{1}{4}}, \quad q_w = \frac{W}{A}, \quad h = \frac{q_w}{\Delta T} \quad (1)$$

where ΔT is the difference between the assembly surface temperature and coolant saturated temperature (K), q_w is the heat flux at the assembly surface (kcal/m²/h), p is the pressure (ata), W is the assembly generation power (kcal/h), and A is the heat transfer area (m²).

The Comparison between Fig. 2 (a) and (b) shows that the maximum temperature on the fuel pellet center can be reduced by decreasing the diameter of the fuel pellets and increasing the number of fuel stacks.

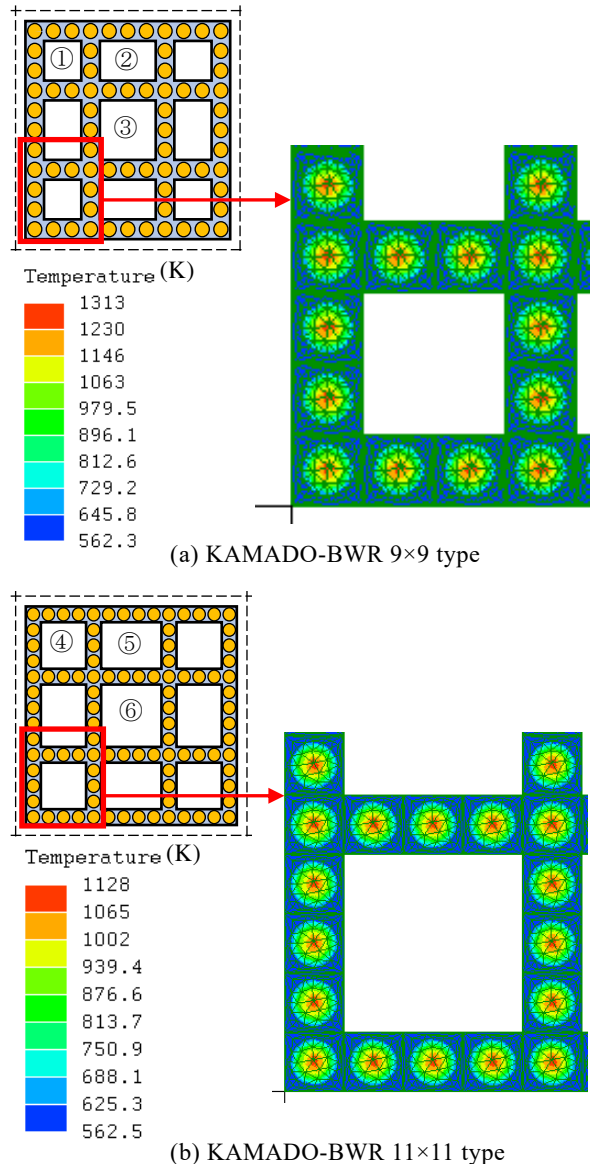


Fig. 2 Temperature distributions in the KAMADO-BWR.

3. Thermal-hydraulic analyses

The pressure drop F_p (Pa/m) with friction pressure of the fuel assembly in the single-phase flow of water is generally

expressed by the Darcy–Weisbach equation ⁹⁾ in Eq. (2),

$$F_p = \frac{f \rho_m U^2}{D} \quad (2)$$

where f is the coefficient of friction, D is the equivalent hydraulic diameter (m), U is the fluid velocity (m/s) and ρ_m is the water density (kg/m³). The f is calculated by the Nikulase equation in Eq. (3) that can be applied with $10^5 < Re < 10^8$, where Re is the Reynolds number,

$$f = 0.0032 + 0.221Re^{-0.237} \quad (3).$$

The U is calculated from the coolant mass flow and the flow path area inside of the fuel assemblies. The U values are 2.60, 3.04 and 2.41 (m/s) for the BWR 9×9, KAMADO-BWR 9×9 type and 11×11 type respectively. As the F_p depends on the D shown in Table 2 for each flow path ① - ⑥ in Fig. 2, and the F_p calculated with Eq. (2) are listed in Table 2.

In the KAMADO-BWR, friction pressure of the fuel assembly is about 1/2 - 1/4 of that in the BWR 9×9. The static pressure multiplied by height is 26.8 kPa for 3.71 m. The pressure drop in the two-phase flow with friction pressure is about 100 times higher than that in water ⁹⁾, which is on the order of MPa in the BWR 9×9 fuel assembly.

The critical heat flux (CHF: q_c) in the two-phase flow was evaluated by the Katto's equation ¹⁰⁾ in Eq. (4),

$$\frac{q_c}{GH_{fg}} = c \left(\frac{\sigma \rho_m U^2}{G^2 L} \right)^{0.043} D/L \quad (4)$$

$$C = 0.25 \quad L/D < 50,$$

$$= 0.25 + 0.0009(L/D - 50) \quad 50 \leq L/D < 150,$$

$$= 0.34 \quad L/D \geq 150$$

where L is the assembly height (m), G is mass velocity (kg/m²/sec), H_{fg} is the heat of vaporization (kJ/kg), σ is the surface tension (N/m) and C is the coefficient changing with L/D .

The q_c is 2.15 MW/m² for the BWR 9×9 and 3.79 - 5.51 MW/m² for KAMADO-BWR according to the flow path shown in Fig. 2. The Details are summarized in Table 2.

Table 2 Pressure drop and CHF for each flow path.

Type	D (m)	F_p (kPa/m)	q_c (MW/m ²)	Q (MW)
BWR	0.0147	2.4253	2.1451	19.7
(a)-①	0.0253	1.6928	4.2244	16.6
(a)-②	0.0303	1.3662	4.7387	18.6
(a)-③	0.0379	1.0515	5.5101	21.6
(b)-④	0.0298	0.9156	3.7920	16.7
(b)-⑤	0.0340	0.7825	4.1426	18.3
(b)-⑥	0.0397	0.6529	4.6100	20.3

The CHF of the KAMADO-BWR is larger than that of the BWR, but it is necessary to consider the heat transfer area. The critical heat output Q of the assembly multiplied by the

heat transfer area in the fuel assembly is 19.7 MW for the BWR 9×9, and 16.6 - 21.6 MW for the KAMADO-BWR. The Q can be adjusted by changing the dimensions of flow path in the KAMADO-BWR assembly. Accordingly, the CHF of the KAMADO-BWR is equivalent to that of the BWR 9×9.

4. Mechanical stress analyses

In terms of structural strength, the tensile strength of SiC (approximately 200 MPa) is equivalent to that of metal materials (200 - 500 MPa). During the assembly loaded in the BWR, the reactor pressure (7 MPa) applies compressive stress to the SiC block and fuel stacks. The stack internal pressure by enclosed He is set to 1 MPa during manufacturing and 2 MPa during operation. The calculation results of the KAMADO-BWR 9×9 and 11×11 types with LISA are shown in Fig. 3 (a) and (b). Although there are some tensile stresses (positive values), most of them are compressive stresses (negative values). The compressive stress is not a problem in terms of the compressive stress limit of SiC (2000 MPa or more).

During unloading the assembly from BWR, the tensile stress on the SiC block is generated by the enclosed He pressure (1MPa) inside the fuel stack. The maximum stress is 3.5 MPa for the KAMADO-BWR 9×9, and 4.7 MPa for the KAMADO-BWR 11×11 types, respectively as shown in Fig. 4 (a) and (b). There are sufficient margins for the tensile strength (approximately 200 MPa).

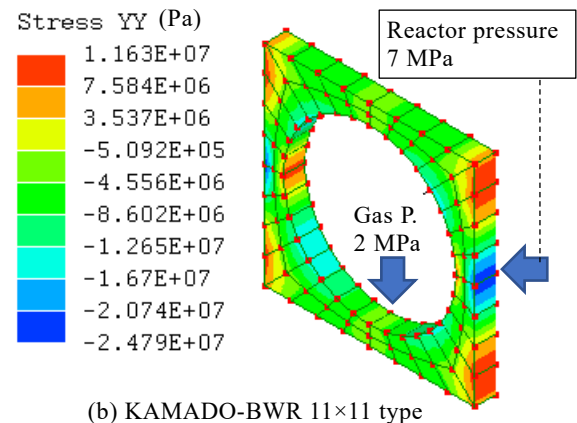
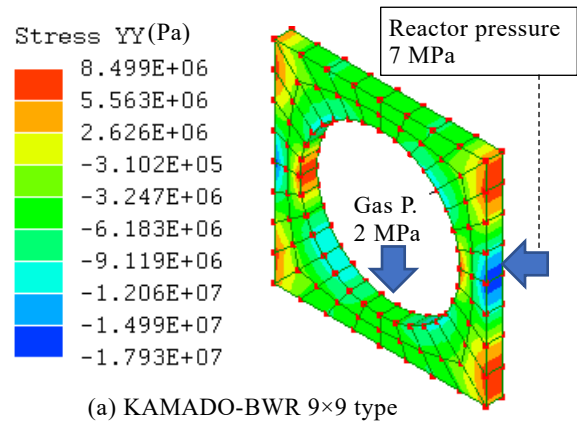


Fig. 3 Stress distributions on SiC block during loading.

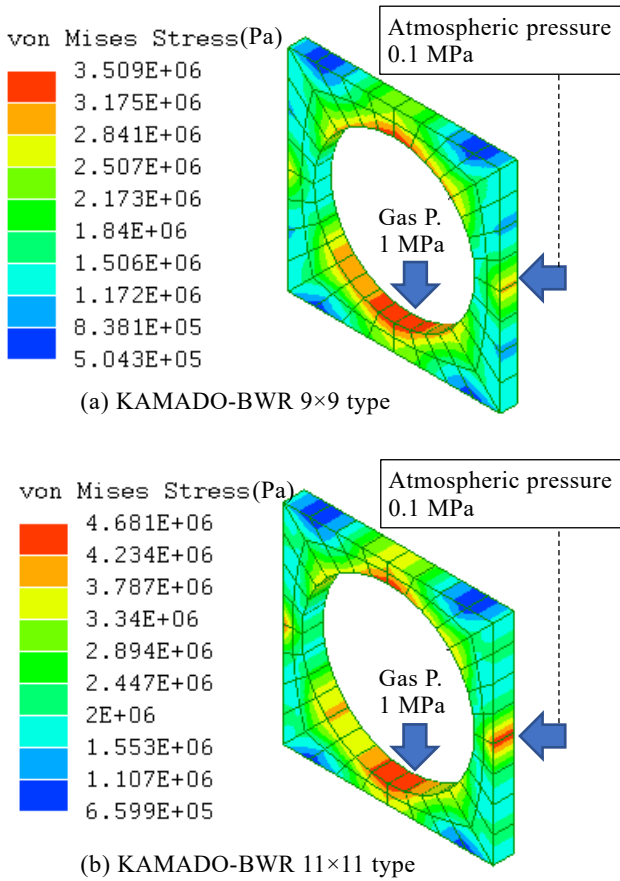


Fig. 4 Stress distributions on SiC block during unloading.

5. Neutron reaction analyses

In neutron reaction calculations, the compositions of UO₂ fuel with 4% enrichment are listed in Table 3. The Monte Carlo codes MVP3¹¹⁾ and MVP-BURN¹²⁾ were used for these calculations.

Table 3 Fuel nuclide composition¹³⁾.

Nuclide	Number density (1/barn/cm)
²³⁴ U	8.0530E-6
²³⁵ U	8.8880E-4
²³⁶ U	5.4190E-6
²³⁸ U	2.1040E-2
O (Natural)	4.4380E-2

Infinite neutron multiplication factors (*k-inf.*) of the fuel assemblies for the commercial BWR 9x9, the KAMADO BWR 9x9 and 11x11 type with void ratios (0, 40, 70%) at the beginning of life (BOL) are summarized in Table 4, assuming that ²³⁵U enrichment for all the pellets in three assemblies is homogeneous, 4% here.

The *k-inf.* depends on the nuclide number density ratio of hydrogen to uranium (H/U), as shown in Fig.5. Comparing the values at 40% void ratio, the *k-inf.* increased as the H/U increase, in ascending order of the KAMADO-BWR 9x9 type, 11x11 type and commercial BWR 9x9. The *k-inf.* and H/U can be adjusted by U loading weight of pellets or water area in

each SiC block. It is also necessary to consider the effect of doped Gd concentration and the average void ratio.

Table 4 *k-inf.* at BOL with void ratios.

Assembly type	Void (%)	H/U	<i>k-inf.</i>
BWR 9x9	0	7.0661	1.4308
	40	5.2965	1.4173
	70	3.9694	1.4011
(a) KAMADO-BWR 9x9 type	0	5.0771	1.4189
	40	3.7908	1.3830
	70	2.8261	1.3296
(b) KAMADO-BWR 11x11 type	0	6.1389	1.4348
	40	4.4689	1.4060
	70	3.2164	1.3544

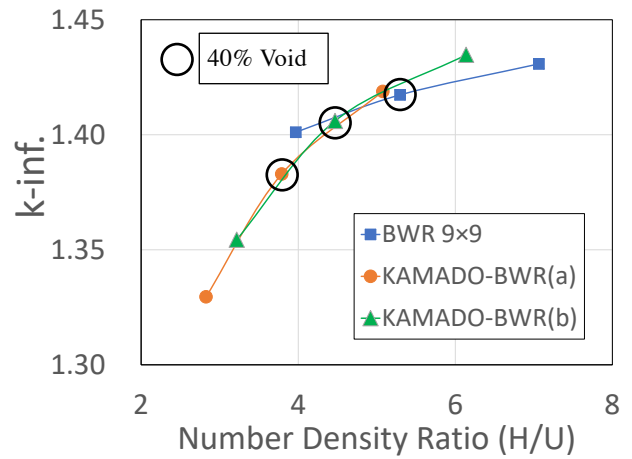


Fig. 5 Changes of *k-inf.* with H/U at BOL.

The *k-inf.* of the fuel assembly for the KAMADO-BWRs is almost the same as that for the commercial BWR as burnup increases (Fig. 6). The *k-inf.* for the KAMADO-BWRs is less than that for the commercial BWR at BOL, while the *k-inf.* for the KAMADO-BWRs becomes greater at the end of life (EOL), because of the higher Pu conversion ratio for them.

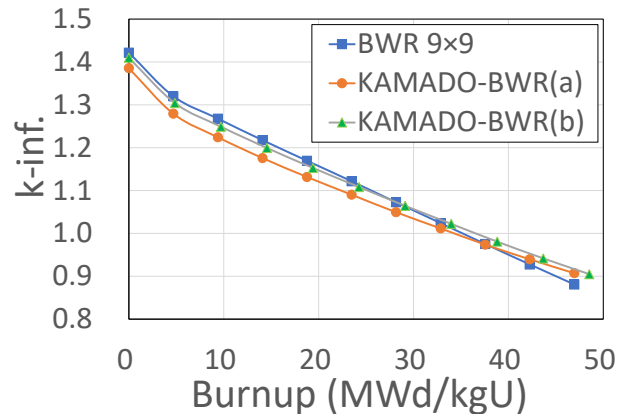
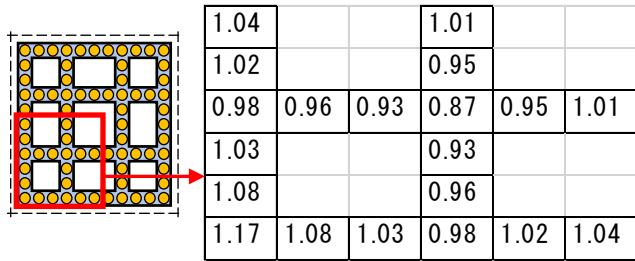


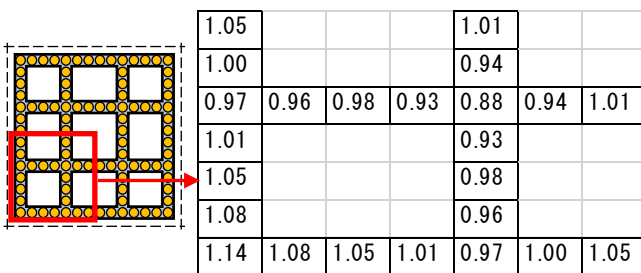
Fig. 6 Changes of *k-inf.* with burnup.

The power distributions of the fuel stack in the KAMADO-BWR are shown in Fig.7, where the void ration is

40% inside and 0% outside the fuel assembly. They are slightly higher at the corner stacks due to the effect of the outside moderator. Although there are further issues such as the effect of Gd fuel, these peaking factors (1.17 or 1.14) may be smaller than that of the commercial BWR fuel assemblies.



(a) KAMADO-BWR 9×9 type



(b) KAMADO-BWR 11×11 type

Fig. 7 Stack power distributions in KAMADO-BWR fuel assemblies.

6. Discussions

SiC materials, fabrication methods, SiC thermal conductivities, superior CHF, severe accident cases for the KAMADO-BWR and application to PWRs are discussed.

6.1 SiC material

SiC materials are known to have high strength but be fragile. For this reason, SiC / SiC composite materials in SiC fibers are researched and developed¹⁴⁾. In addition, there are various methods for manufacturing SiC parts or blocks, such as atmospheric pressure sintering method, hot press method, hot isotropic press (HIP) method, chemical vapor deposition (CVD) method, reaction sintering (RS) method and others. Since the mechanical performance of SiC differs depending on these methods, it is necessary to pay careful attention to the results of research and development for the SiC manufacturing methods¹⁵⁾.

6.2 Fabrication method

SiC parts or blocks can be produced by powder sintering method such as hot press method. However, it is known that some processes such as welding and other joining method is difficult for SiC materials. A trial method without joining processes to fabricate the KAMADO-BWR fuel assembly is suggested and shown in Fig. 8.

The fabricating procedures are as follows:

- 1) manufacture an SiC block with necessary holes for fuel stacks by the powder sintering method,
- 2) insert fuel pellets into the holes in the SiC block,

- 3) cover the block with a seal of swollen graphite that can withstand high temperature,
- 4) put a lid on the seal and tighten them with bolts and nuts.

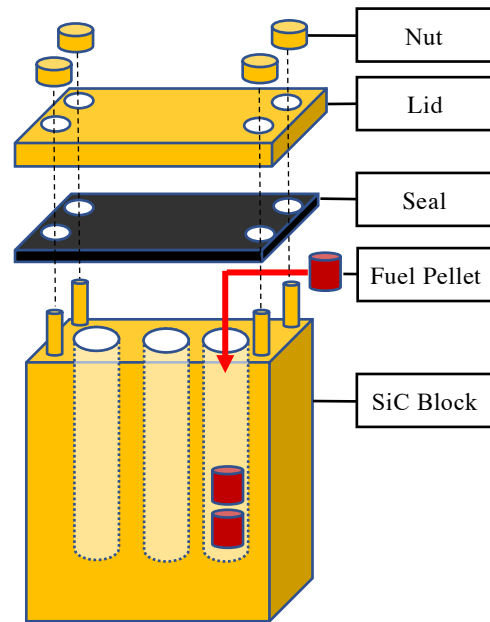


Fig. 8 Fabrication method for KAMADO-BWR fuel assembly.

6.3 Thermal conductivity

It has been reported that the thermal conductivity of SiC deteriorates as irradiation damages in it are accumulated¹⁶⁾. We analyzed the temperature distribution when the thermal conductivity of SiC was reduced to 20 W/m/K, which is 1/10 of that in as-fabricated fresh conditions. Comparing with results in the previous temperature analysis shown in Fig.2 (a), the maximum fuel temperature (1137 K) increased by 39 K at the same assembly power (4.31 MW) as shown in Fig. 9. The temperature increment is slight.

It has been also reported that the thermal conductivity deterioration with irradiation damages depends on the method of manufacturing SiC matrices or making SiC / SiC composite materials¹⁷⁾.

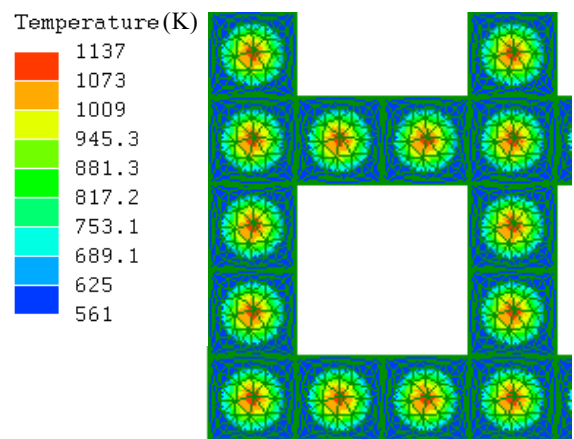


Fig 9 Fuel temperature distribution in KAMADO-BWR 9×9 type at reducing SiC heat conductivity to 20 W/m/K.

6.4 Superior CHF

If the heat flux to the two-phase coolant inside the KAMADO-BWR fuel assembly exceeds the critical heat flux q_c during operation, and if the coolant becomes only steam, major parts of the heat generated at fuel pellets can be removed through the surfaces surrounding the fuel assembly.

The cooling performance by steam was evaluated by the Dittus-Boelter formula⁹⁾ in Eq. (5),

$$h = 0.023Re^{0.8}Pr^{0.4}\lambda/D \tag{5}$$

where Pr is the Prandtl number, λ is the thermal conductivity of steam, and D is the value at flow pass ② in Fig. 2. The h is calculated to be 10.3 kW/m²/K, while the coolant becomes the two-phase flow outside the fuel assembly and the cooling performance is still maintained to be high (94 kW/m²/K). The maximum fuel temperature (1171 K) increased by 73 K at the same assembly power (4.31MW) as shown in Fig. 10. The temperature increment is not large.

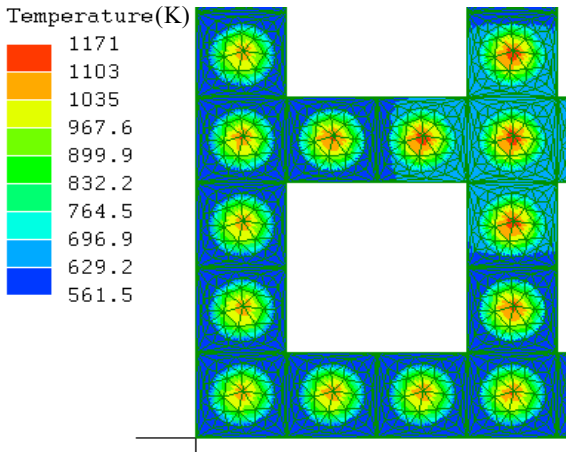


Fig 10 Fuel temperature distribution in KAMADO-BWR 9×9 type beyond CHF condition.

If the heat transfer capability of the flow path is reduced inside the fuel assembly and is maintained outside it, the cooling performance can be ensured. Moreover, if the thermal conductivity of SiC also was reduced to 20 W/m/K, the maximum fuel temperature (1230 K) increased by 132 K at the same assembly power. Consequently, the temperature increment is not significant on the fuel integrity.

6.5 Severe accident

When the cooling water was exhausted in case of the severe accidents, the temperature distribution in the KAMADO-BWR fuel assembly was evaluated assuming the fuel decay heat decreased to 1/10 of the fuel fission reaction energy. There is no cooling inside the assembly, and simple evaluation outside the assembly was carried out with the radiative cooling formula in Eq. (6),

$$h = \sigma_{SB}T^3 \tag{6}$$

where σ_{SB} is the Stefan-Boltzmann constant and T is the surface temperature (K). Assuming that the surface temperature of the assembly is 1500 K, the h becomes 191 W/m²/K. Using the h , the maximum temperature at fuel pellets is 1881 K and the minimum temperature is 1569 K (Fig. 11).

The fuel decay heat in the KAMADO-BWR fuel assembly can be also sufficiently removed by conduction of radiant heat through the SiC block to the coolant. Hence it may be possible to prevent fuel melting in case of severe accidents.

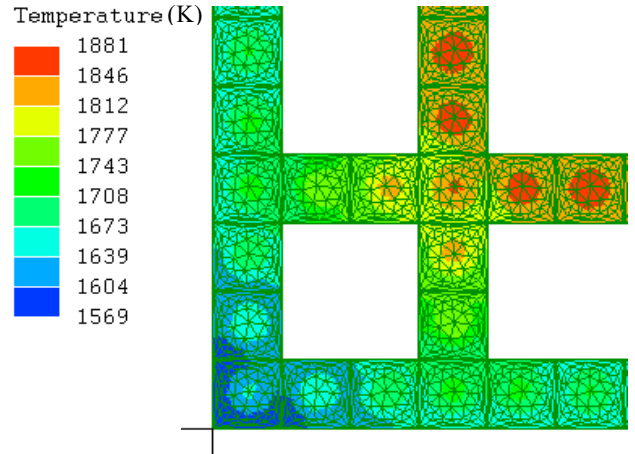


Fig 11 Fuel temperature distribution in KAMADO-BWR 9×9 type during severe accident.

6.6 Application to PWR

Another KAMADO concept can be also applied to commercial PWRs, and the PWR 17×17 type fuel assembly is shown in Fig. 12. The assembly necessarily includes an in-core instrumentation thimble and control rod guide thimbles at the fixed locations in the commercial PWRs. The fuel pellet diameter is 7.8 mm, smaller than 8.2 mm diameter of the commercial PWR fuel pellet, and the number of fuel stacks is 252 less than 264 rods in each PWR assembly. There are still manufactural and mechanical issues to be confirmed, such as stability on inserting or drawing control rods.

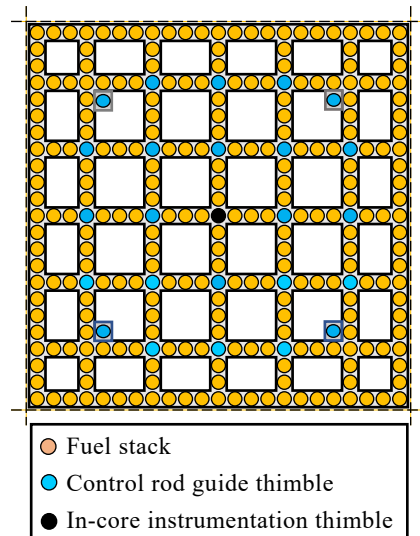


Fig 12. KAMADO-PWR 17×17 type fuel assembly.

7. Conclusions

A new concept of the accident tolerant fuel assembly for the KAMADO-BWR is proposed, and the assembly is composed of an SiC block and conventional UO₂ fuel pellets. The melting point of SiC and UO₂ is higher than 3000 K and these ceramic materials scarcely produce hydrogen with light water coolant. The considerable thermal conductivity of SiC also provides the significant heat transfer from the pellets to the coolant.

Analytical results of the fuel assembly temperature, mechanical stress, thermal-hydraulics and neutron reaction prove that both the KAMADO-BWR 9×9 and 11×11 type assemblies have satisfactory performance equivalent to the commercial BWR 9×9 assembly.

The maximum temperature on the fuel pellet center can be reduced by decreasing the diameter of the fuel pellets and increasing the number of fuel stacks. If the thermal conductivity of SiC deteriorating due to irradiation damage accumulation, the increment in the maximum fuel temperature is slight.

As the friction pressure in the KAMADO-BWR fuel assembly is much less than that in the commercial BWR 9×9 fuel assembly, the pressure drop of flow path in the KAMADO-BWR also becomes the less.

Though the stress on the SiC block is compressive during the reactor operation or tensile while unloading the fuel assemblies, stresses in these conditions are much less than the limit of structural strength of SiC.

Since the KAMADO-BWR 9×9 and 11×11 type assembly have the smaller H/U ratio than that of the commercial BWR 9×9 assembly, the *k-inf.* of the KAMADO-BWR assemblies is less at BOL, while it becomes greater at EOL than that of the commercial BWR because of higher Pu conversion ratio.

Additionally, SiC materials, fabrication methods, SiC thermal conductivities, superior CHF, severe accident cases for the KAMADO-BWR fuel assemblies and application to the PWR 17x17 type assembly are discussed. They are appropriately verified or confirmed.

Accordingly, the concept of KAMADO-BWR assembly is expected to be one candidate of the accident tolerant and replacement fuel assemblies for commercial BWRs or ABWRs.

References

- 1) OECD/NEA No. 7317: State-of-the-Art Report on Light Water Reactor Accident-Tolerant Fuels (2018).
- 2) IAEA-TECDOC-1797: Accident Tolerant Fuel Concepts for Light Water Reactors, Proceedings of a Technical Meeting Held at Oak Ridge National Laboratories, United States of America, 13–16 October 2014 (2018).
- 3) Tetsuo MATSUMURA, Takanori KAMEYAMA, Yasushi NAUCHI and Izumi KINOSHITA: A New Passive Safety FBR Concept of “KAMADO” – Easy Replacement from the Existing Light Water Reactor to FBR”, ICAPP 9370, Tokyo, Japan (2009).
- 4) IAEA-TECDOC-1485: Status of Innovative Small and Medium Sized Reactor Designs 2005 - Reactors with Conventional Refueling Schemes – (2006).
- 5) IAEA Advanced Reactors Information Systems (ARIS), <https://aris.iaea.org/>.
- 6) Toshiyasu MIYASHITA, Nobuo NAKAE, Keizo OGATA, Toshikazu BABA, Katsuichiro KAMIMURA, Hitoshi MATSUOKA and Kazuo KAKIUCHI: Verification Program of BWR 9×9 Fuel, Transactions of the Atomic Energy Society of Japan, Vol. 7, No. 4, pp. 380-395 (2008) [in Japanese].
- 7) LISA Finite Element Analysis, Sonnenhof Holdings, <https://www.lisafea.com/index.html>.
- 8) W. H. Jens, P. A. Lottes: Analysis of Heat Transfer, Pressure Drop and Density Data for High Pressure Water, ANL-4627 (1951).
- 9) JSME Heat Transfer Handbook, JSME (1993).
- 10) Yoshiro KATTO: 一樣加熱垂直円管内の強制流動沸騰限界熱流束の研究, 45, 400, 1892-1901. Transactions of the JSME (1979) [in Japanese].
- 11) Yasunobu NAGAYA, Keisuke OKUMURA, Takeshi SAKURAI and Takamasa MORI: MVP/GMVP Version 3: General Purpose Monte Carlo Codes for Neutron and Photon Transport Calculations Based on Continuous Energy and Multigroup Methods, JAEA-Data/Code 2016-019 (2016).
- 12) Keisuke OKUMURA, Takamasa MORI, Masayuki NAKAGAWA and Kunio KANEKO: Validation of a Continuous-energy Monte Carlo Burn-up Code MVP-BURN and Its Application to Analysis of Post Irradiation Experiment, J. Nucl. Sci. Technol., 37, pp. 128 (2000).
- 13) Keisuke OKUMURA, Kazuteru SUGINO, Kensuke KOJIMA, Tomoyuki JIN, Tsutomu OKAMOTO and Junichi KATAKURA: A Set of ORIGEN2 Cross Section Libraries Based on JENDL-4.0: ORLIBJ40, JAEA-Data/Code-2012-032 (2013).
- 14) Walter Krenkel: Carbon Fibre Reinforced Silicon Carbide Composites (C/SiC, C/C-SiC), Handbook of Ceramic Composites, Springer, Boston, MA (2005).
- 15) Shoko SUYAMA, et al.: High-Strength, Reaction-Sintered Silicon Carbide Ceramic, Toshiba review, Vol.58 No. 5 (2003) [in Japanese].
- 16) Akira HASEGAWA: Neutron Irradiation Effects of SiC and SiC/SiC Composite, Journal of Plasma and Fusion Research Vol.80, No.1 pp. 24-30 (2004) [in Japanese].
- 17) Yutai KATOH: Status and Prospects of SiC-Based Ceramic Composites for Fusion and Advanced Fission Applications, Journal of Plasma and Fusion Research Vol.80, No.1 January pp. 18-23 (2004) [in Japanese].

Generation of Ammonium Ions in Water by Atmospheric-pressure Argon Plasma Jet Irradiation at Room Temperature

by

Hiroshi KUWAHATA^{1*} and Ikko MIKAMI²

(Received on Mar. 29, 2022 and accepted on May 27, 2022)

Abstract

Ammonium ions (NH_4^+) were generated in water irradiated with an atmospheric-pressure argon (Ar) plasma jet in air at room temperature. The concentration of NH_4^+ in the water was measured using a capillary electrophoresis (CE) system under different plasma irradiation conditions [plasma irradiation duration, 20–80 min; applied voltage, 8–10 kV; plasma irradiation distance (position of the water surface), 2–40 mm]. The NH_4^+ concentration in the water increased approximately in proportion to the plasma irradiation duration and applied voltage. The maximum NH_4^+ concentration was 43.2 μM when the applied voltage was 10 kV, the Ar gas flow rate was 10 L/min, the plasma irradiation distance was 10 mm, and the plasma irradiation duration was 80 min. The power consumption during plasma irradiation was ~ 20 W.

Keywords: Atmospheric-pressure plasma, Ammonium ions, Capillary electrophoresis

1. Introduction

Ammonia (NH_3) is used in the synthesis of various chemical products such as fertilizers, explosives, plastics, and synthetic fibers and resins¹⁻³. According to a research report of the United States Geological Survey (USGS), the annual world total production of NH_3 was ~ 96 million tons in 1995, ~ 104 million tons in 2000, ~ 131 million tons in 2010, and ~ 150 million tons in 2019, showing a yearly increase⁴⁻⁶. Approximately 80% of the produced NH_3 is used in the manufacture of fertilizers^{7,8}. NH_3 is a chemically synthesized product that is indispensable for producing the food essential for our survival. NH_3 is also expected to be used as a hydrogen carrier for fuel cells, which are necessary for the realization of a hydrogen-energy-based society, and as an easy-to-handle energy source that can be easily liquefied⁹⁻¹¹.

The current industrial synthesis of NH_3 is generally based on the Haber–Bosch process¹⁻³. In 1909, Haber succeeded in synthesizing NH_3 by reacting nitrogen gas (N_2) with hydrogen gas (H_2) using osmium (Os) as a catalyst at 500–600 °C and 200 atm¹². The industrialization of NH_3 synthesis was promoted by Bosch and coworkers at BASF in Germany, and in 1912, Mittasch and coworkers at BASF successfully synthesized NH_3 using a triiron tetroxide (Fe_3O_4) catalyst mixed with 2–6% alumina (Al_2O_3) and 0.2–0.6% potassium oxide (K_2O) instead of an Os catalyst at a decreased temperature (450 °C) and pressure (100 atm)^{13,14}.

The Haber–Bosch process is a high-temperature, high-

pressure process that consumes much energy, which led to a search for catalysts to lower the temperature and pressure in the synthesis process¹⁵. In 1971, Ozaki *et al.* achieved a reduced temperature (146 °C) and pressure (600 mmHg) using a ruthenium (Ru)-carbon (C)-potassium (K) catalyst instead of an iron-based catalyst¹⁶. In 2003, Yandulov and Schrock reported the synthesis of NH_3 at room temperature and 1 atm using a molybdenum (Mo) nitrogen complex with a triamide monoamine tetradentate ligand¹⁷. Since this report, many researchers have reported the synthesis of NH_3 at room temperature and 1 atm using various catalysts.

H_2 gas is used in the Haber–Bosch process and must be produced for the synthesis of NH_3 . H_2 gas is mainly produced by reforming natural gas. In plants for NH_3 synthesis, the production process of H_2 gas accounts for a large part of the entire process, and more than 90% of the total energy consumption of the NH_3 synthesis process is spent on the production of H_2 gas. The process of NH_3 synthesis including the production of H_2 gas makes up 1–2% of the total energy consumption by human beings¹⁸. Therefore, if NH_3 can be synthesized without using H_2 gas, energy consumption will be greatly reduced.

A method of NH_3 synthesis at room temperature without catalysts and H_2 gas was reported by Haruyama *et al.* in 2016¹⁹. By combining ultraviolet (UV) light irradiation and an atmospheric-pressure air plasma or N_2 plasma, they successfully generated NH_3 in water using water instead of H_2 gas.

An atmospheric-pressure plasma is generated under atmospheric pressure, as indicated by its name. Compared with low-pressure plasmas, atmospheric-pressure plasmas are characterized by an electron temperature being higher than the

*1 Associate Professor, Department of Electrical and Electronic Engineering

*2 Associate Professor, Department of Chemistry

ion temperature in the plasma as well as a high electron energy^{20,21}). Research on the surface treatment of solid materials²²⁻²⁴), the purification of water^{25,26}), and the inactivation of bacteria and fungus^{27,28}) has been carried out using atmospheric-pressure plasmas. In particular, atmospheric-pressure plasmas have recently been used in biomedical applications^{29,30}), such as cancer treatment^{31,32}), and the intracellular introduction of genes and drug molecules^{33,34}), which has been intensively studied.

In our laboratory, we have been studying the decolorization of colored wastewater using an atmospheric-pressure argon (Ar) plasma jet³⁵⁻³⁷). We previously reported that hydrogen peroxide (H_2O_2)^{38,39}) as well as nitric acid (HNO_3) and nitrous acid (HNO_2)^{40,41}) were formed in distilled water irradiated with an atmospheric-pressure Ar plasma jet. In these studies, the possibility of nitrogen (N) radicals being formed through the dissociation of N_2 molecules in the air was discussed as a cause of the formation of HNO_3 and HNO_2 . NO_3 and NO_2 are formed because of the oxidation reaction of N radicals. oxygen (O) radicals, which are necessary for the oxidation reaction, should be formed by the dissociation of oxygen molecules (O_2) in air. It was considered that the N and O radicals combine to form NO_3 and NO_2 . The dissociation of N_2 and O_2 molecules is considered to be caused by high-energy electrons in the plasma. When the high-energy electrons collide with water (H_2O) molecules, the H_2O molecules are dissociated into hydrogen (H) and hydroxyl (OH) radicals. The OH radicals combine with each other to form H_2O_2 . Recently, we predicted that NH_3 can be produced when N and H radicals combine.

In this paper, we report that NH_3 is formed in distilled water irradiated with an atmospheric-pressure Ar plasma jet in air. The dependences of the concentration of ammonium ions (NH_4^+) in the distilled water on the plasma irradiation duration, applied voltage, Ar gas flow rate, and plasma irradiation distance were determined. The temperature of the distilled water during plasma irradiation was also measured using a thermocamera.

2. Experimental methods

Figure 1 shows a schematic of the experimental setup used in this study. In the unit that generates a plasma jet, a discharge electrode made of a copper tube (inner diameter, 4 mm; outer diameter, 6 mm) was inserted into a dielectric quartz tube (length, 50 mm; inner diameter, 6 mm; outer diameter, 8 mm) wrapped with copper foil (thickness, 0.05 mm; width, 10 mm) that functioned as the ground electrode. A high AC voltage was applied to the electrodes to induce dielectric barrier discharge inside the quartz tube between the electrodes and to convert the introduced Ar gas to plasma that was then ejected into air in the form of a jet. The plasma jet was generated at a frequency of 10 kHz and an applied voltages of 8-10 kV using a high-voltage power supply (LHV-10AC, Logy Electric Co., Ltd.). Distilled water (20 mL) in a glass Petri dish of 60 mm diameter was irradiated with the plasma jet at distances of 2-40 mm (from the end of the quartz tube to the liquid surface) for 0-80 min. Ar gas was adjusted the gas flow rate of 10 L/min using a gas flow meter (RK-1250, Kofloc). Voltage and current were measured using a digital oscilloscope (TDS1001B,

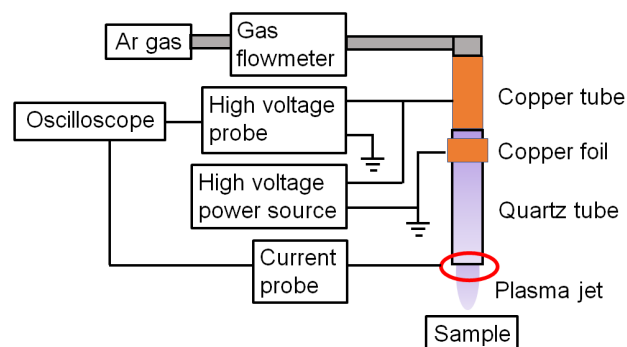


Fig. 1 Schematic of experimental setup.

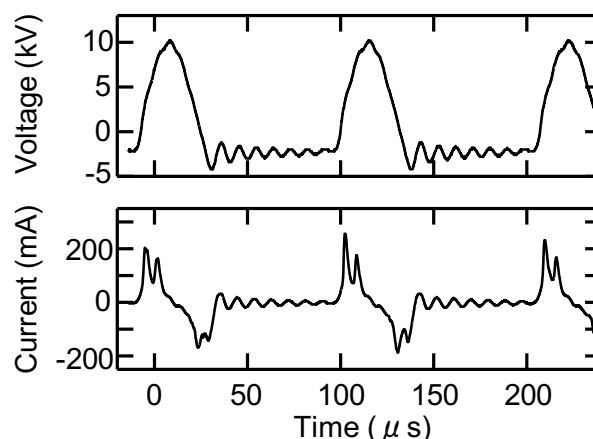


Fig. 2 Typical waveforms of voltage and current (applied voltage, 10 kV; irradiation distance, 15 mm).

Tektronix, Inc.), a high-voltage probe (P6015A, Tektronix, Inc.), and a current probe (A621, Tektronix, Inc.). Power consumption during plasma irradiation was measured using a watt monitor (TAP-TST8N, Sanwa Supply Inc.).

Nessler's reagent was used to confirm the presence of NH_3 in the distilled water. A capillary electrophoresis (CE) system (G1602A, Agilent Technologies Japan, Ltd.) was used to measure the NH_4^+ concentration in the distilled water. NH_3 is present as NH_4^+ in the distilled water. As the electrophoresis solution, a mixed solution of 10 mM imidazole, 5 mM lactic acid, and 0.5 mM 18-crown-6 was prepared, with the pH adjusted to 4.5 using 1 M acetic acid. Fused silica tubes with an inner diameter of 50 μm were used as the capillary tubes. The NH_4^+ was detected by the indirect absorbance method with an applied voltage of 30 kV, a detection wavelength of 310 nm (bandwidth of 20 nm), and a control wavelength of 215 nm (bandwidth of 10 nm).

A thermocamera (F30, NEC Avio Infrared Technologies) was used to measure the temperature of the distilled water during plasma irradiation.

3. Results and discussion

Figure 2 shows typical voltage and current waveforms during plasma irradiation. In the voltage waveform, a pulse with a maximum voltage of 10 kV and a maximum width of

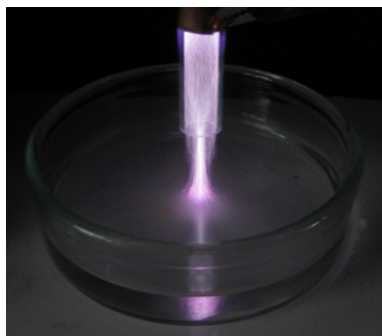


Fig. 3 Photograph of plasma jet ejected onto distilled water (applied voltage, 10 kV; irradiation distance, 15 mm).

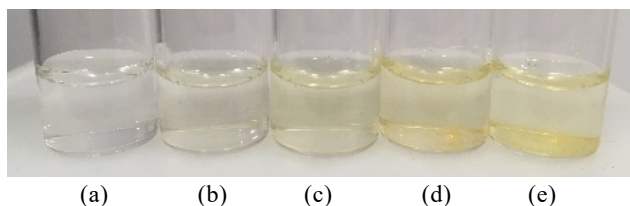


Fig. 4 Reaction of Nessler's reagent for different plasma irradiation durations (applied voltage, 10 kV; irradiation distance, 15 mm); (a) 0 min, (b) 20 min, (c) 40 min, (d) 60 min, and (e) 80 min.

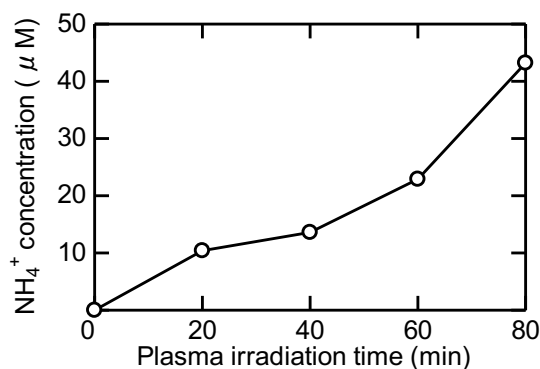


Fig. 5 Dependence of NH₄⁺ concentration on plasma irradiation duration (applied voltage, 10 kV; irradiation distance, 15 mm).

~33 μs appears once every 100 μs (because the power source frequency is 10 kHz). In the current waveform, the peaks were observed at the rise and fall of the voltage in the voltage waveform, and the maximum and minimum currents were 380 and -220 mA, respectively. This suggested that discharge occurred twice in 100 μs. The positive and negative currents were considered to be due to Ar⁺ ions and electrons, respectively. The time between the positive currents and the negative currents were ~25 μs. The power consumption during the irradiation of the plasma to the distilled water was ~20 W.

Figure 3 shows the plasma ejected onto the distilled water. There were many streamers in the plasma, which looked like white lines and collided with the distilled water. Therefore, it is considered that both Ar⁺ ions and electrons in the plasma reached the surface of the distilled water.

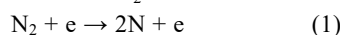
Figure 4 shows the reaction of Nessler's reagent for

different plasma irradiation durations. The color of the reagent was pale brown after 20 min of irradiation and became darker with increasing plasma irradiation duration. This result indicates that NH₄⁺ was present in the distilled water owing to plasma irradiation and that its concentration increased with the plasma irradiation duration.

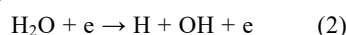
Figure 5 shows the dependence of the NH₄⁺ concentration in the distilled water on the plasma irradiation duration. The NH₄⁺ concentration in the distilled water increased almost in proportion to the plasma irradiation duration and was 43.2 μM after 80 min of irradiation.

Haruyama *et al.* used UV irradiation (185 and 254 nm) and an atmospheric-pressure N₂ plasma to produce 18 μM NH₄⁺ in water in 20 min¹⁹). Although this concentration was ~1.7-fold higher than our result (10.4 μM) obtained by irradiation for 20 min, they had used N₂ gas instead of air. If we also use N₂ gas instead of air, the NH₃ concentration is expected to increase. However, we prefer to use air as it is.

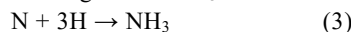
The following is a possible synthesis process of NH₃ and NH₄⁺ using an atmospheric-pressure plasma. High-energy electrons (e) in the plasma collide with N₂ molecules in air, which causes N₂ to be dissociated into N radicals^{42, 43}.



In addition, the high-energy electrons (e) in the plasma also collide with H₂O molecules on the surface of the distilled water, causing H₂O to be dissociated into H and OH radicals^{44, 45}.



The N and H radicals combine on the surface of the distilled water and generate NH₃ in air.



Part of this NH₃ diffuses into air and the remainder dissolves in the distilled water.

The H₂O in the distilled water is ionized into H ions (H⁺) and OH ions (OH⁻).



In the distilled water, NH₃ combines with H⁺ to form NH₄⁺.



The dissociation energies of N₂ and H₂O molecules are 9.1 eV⁴⁶) and 5.1 eV^{46,47}), respectively. If N₂ molecules are dissociated, the electrons in our atmospheric-pressure Ar plasma jet are considered to have a potential energy of ≥9.1 eV.

Haruyama *et al.* synthesized NH₃ in water by simultaneously irradiating the water with UV light and an atmospheric-pressure N₂ or air plasma and considered that the electrons in the plasma had a potential energy of ≥9.1 eV¹⁹). Their result supports our discussion.

On the other hand, Ar atoms in the metastable state are considered to also exist in the Ar plasma. The Ar atoms in the metastable state have an energy of 11.5 eV^{48,49}). They might have collided with N₂ and H₂O to dissociate these molecules.

Figure 6 shows the dependence of the NH₄⁺ concentration in the distilled water on the applied voltage when the irradiation distance was 15 mm and the irradiation duration was 60 min. With applied voltage of ≥8 kV, the NH₄⁺ concentration increased approximately in proportion to the applied applied voltage and was 23 μM for an applied voltage

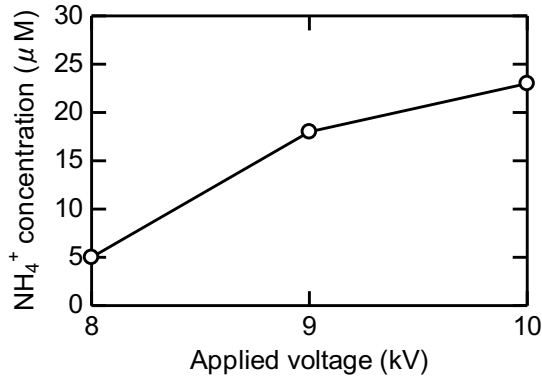


Fig. 6 Dependence of NH₄⁺ concentration on applied voltage (irradiation distance, 15 mm; irradiation duration, 60 min).

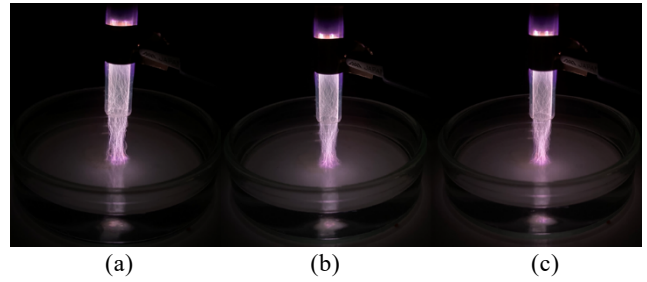


Fig. 7 Photographs of the plasma jet ejected onto the distilled water for different applied voltages when the irradiation distance was 15 mm; (a) 8 kV, (b) 9 kV, and (c) 10 kV.

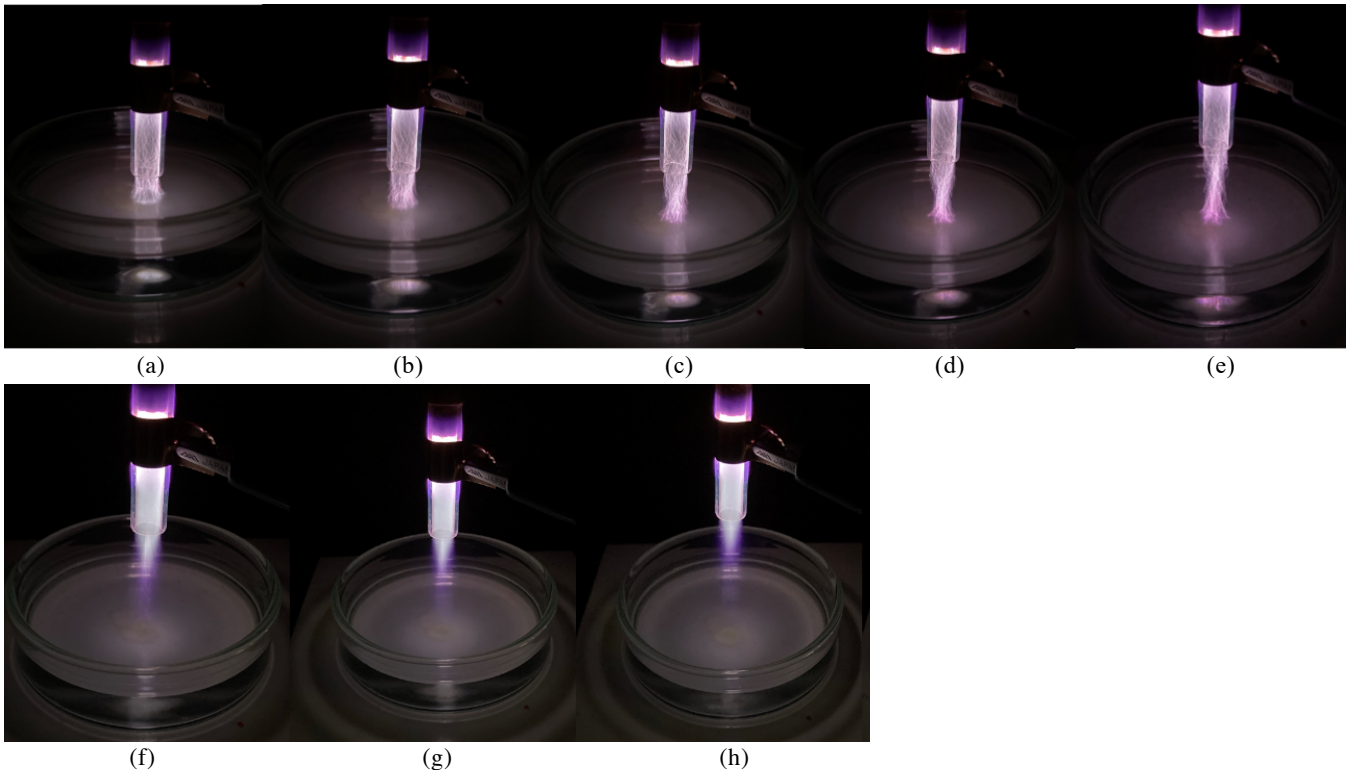


Fig. 8 Photographs of plasma jet ejected onto distilled water for different irradiation distances when the applied voltage was 10 kV; (a) 2 mm, (b) 5 mm, (c) 10 mm, (d) 15 mm, (e) 20 mm, (f) 25 mm, (g) 30 mm, and (h) 40 mm.

of 10 kV. This may be because the number of ionized Ar atoms increased with the applied voltage, which then increased the number of electrons and thereby the numbers of N and H radicals, resulting in an increased number of NH₃ molecules.

Figure 7 shows photographs of the plasma jet ejected onto the distilled water for different applied voltages when the irradiation distance was 15 mm. The streamers reached the water surface at all applied voltages. There were no differences in the behavior of the plasma jet when it came in contact with the water surface.

Figure 8 shows photographs of the plasma jet ejected onto the distilled water at different irradiation distances when the applied voltage was 10 kV. When the irradiation distance was 2 mm [Fig. 8(a)], the streamer traveled straight from the quartz tube and reached the water surface. When the

irradiation distance was 5-20 mm [Figs. 8(b)-8(e)], some streamers were slightly focused and they reached the water surface. When the irradiation distance was 25-40 mm [Figs. 8(f)-8(h)], the streamers were indistinct and did not appear to reach the water surface. From these results, we found that whether the streamers reach the water surface and the state of the plasma both depend on the plasma irradiation distance.

Figure 9 shows the dependence of the NH₄⁺ concentration in the distilled water on the plasma irradiation distance. The NH₄⁺ concentration was 12 μM for an irradiation distance of 2 mm, increased with irradiation distance to reach a maximum of 22 μM for 10 mm, and then decreased for 15-20 mm. The NH₄⁺ concentration remained almost unchanged for 25-40 mm. These results indicate that the NH₄⁺ concentration in the distilled water depends on the plasma irradiation distance and

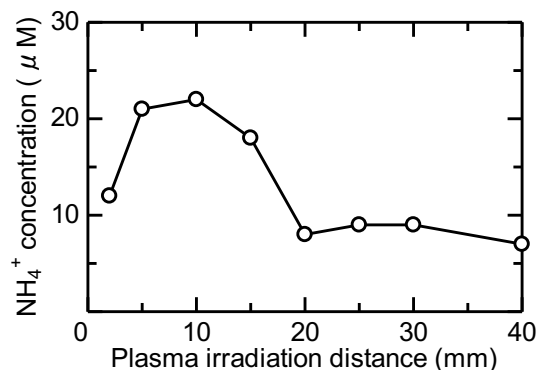


Fig. 9 Dependence of the NH_4^+ concentration in the distilled water on the plasma irradiation distance (applied voltage, 10 kV; irradiation duration, 60 min).

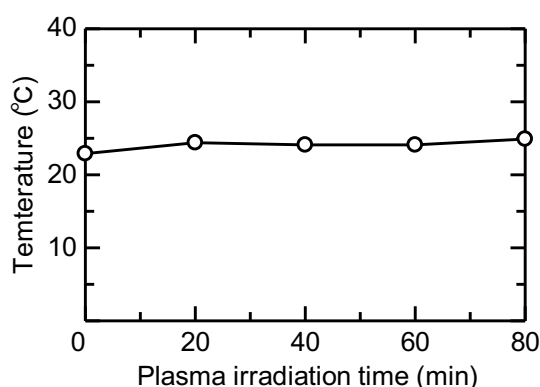


Fig. 10 Dependence of temperature of distilled water, determined by thermography, during plasma irradiation on plasma irradiation duration (applied voltage, 10 kV; irradiation distance, 15 mm).

reaches a maximum at an irradiation distance of 10 mm. The reason for this is considered to be as follows. Because the field of NH_3 synthesis expressed by Eq. (3) is in the vicinity of the water surface, the number of generated H radicals increases with decreasing plasma irradiation distance, resulting in an increased NH_4^+ concentration. However, the distance over which the plasma reacts with air is short when the plasma irradiation distance is excessively short. As a result, the amount of generated N radicals decreases and the NH_4^+ concentration also decreases. For an irradiation distance of 20 mm [Fig. 8(e)], the streamer reached the water surface. However, the NH_4^+ concentration for 20 mm was equivalent to those for other irradiation distances [Figs. 8(f)-8(i)] in which the streamers did not appear to reach the water surface. The reason for this remains unclear.

Figure 10 shows the dependence of the temperature of the distilled water, which was determined by thermography, during plasma irradiation on the plasma irradiation duration. The temperature of the distilled water was 22.9 °C at the start of plasma irradiation and was 24.9 °C after irradiation for 80 min. This result indicates that the temperature of the distilled water increased by ~1.5 °C owing to the initial plasma irradiation but remained almost unchanged at around room temperature during irradiation.

4. Conclusions

NH_4^+ were synthesized in distilled water irradiated with an atmospheric-pressure Ar plasma jet in air at room temperature. This is a result of N radicals dissociating from N_2 in air and H atoms dissociating from H_2O on the surface of the distilled water combining to become NH_3 , which dissolved in the distilled water and combined with H^+ in the water. The NH_4^+ concentration in the distilled water increased approximately proportionally to the plasma irradiation duration and applied voltage. In our experiment, the maximum NH_4^+ concentration of 43.2 μM was obtained when the applied voltage was 10 kV, the Ar gas flow rate was 10 L/min, the plasma irradiation distance was 10 mm, and the plasma irradiation duration was 80 min. The power consumption during plasma irradiation was ~20 W.

References

- 1) J. R. Jennings, *Catalytic Ammonia Synthesis. Fundamentals and Practice*, (Plenum Press, New York, 1991).
- 2) A. Nielsen, *Ammonia: Catalysis and Manufacture* (Springer, Heidelberg, 1995).
- 3) M. Appl, *Ammonia: Principle and Industrial Practice* (Wiley-VCH, Weinheim, 1999).
- 4) Mineral commodity summaries, U. S. Geological Survey (USGS) Report 2001.
- 5) Mineral commodity summaries, U. S. Geological Survey (USGS) Report 2011.
- 6) Mineral commodity summaries, U. S. Geological Survey (USGS) Report 2020.
- 7) J. N. Galloway, A. R. Townsend, J. W. Erismann, M. Bekunda, Z. Cai, J. R. Freney, L. A. Martinelli, S. P. Seitzinger, and M. A. Sutton, Transformation of the Nitrogen Cycle: Recent Trends, Questions, and Potential Solutions, *Science* Vol.320, pp.889-892 (2008).
- 8) J. W. Erismann, M. A. Sutton, J. Galloway, Z. Klimont, and W. Winiwarter, How a century of ammonia synthesis changed the world, *Nature Geoscience* Vol.1, pp.636-639 (2008).
- 9) F. Vitse, M. Cooper, and G. G. Botte, On the use of ammonia electrolysis for hydrogen production, *Journal of Power Sources* Vol.142, pp.18-26 (2005).
- 10) T. Saika, M. Nakamura, T. Nohara, and S. Ishimatsu, Study of hydrogen supply system with ammonia fuel, *JSME International Journal* Vol.B49, pp.78-83 (2006).
- 11) C. Zamfirescu and I. Dincer, Ammonia as a green fuel and hydrogen source for vehicular applications, *Fuel Processing Technology* Vol.90, pp.729-737 (2009).
- 12) F. Haber, *The Synthesis of Ammonia from its Elements*, Nobel Lecture 1920; available at www.nobelprize.org/nobel_prizes/chemistry/laureates/1918/haber-lecture.pdf.
- 13) A. Mittasch, *Advances in Catalysis* Vol. II, ed. W. G. Frankenburg (Academic Press, New York, 1950).
- 14) W. G. Frankenburg, *Catalysis* Vol. III, ed. P. H. Emmett (Reinhold Pub. Corporation, New York, 1955).
- 15) Y. Nishibayashi, Molybdenum-catalyzed reduction of molecular dinitrogen under mild reaction conditions,

- Dalton Transactions Vol.41, pp.7447-7453 (2012).
- 16) A. Ozaki, K. Aika, and H. Hori, A new catalyst system for ammonia synthesis, Bulletin of the Chemical Society of Japan Vol.44, p.3216 (1971).
 - 17) D. V. Yandulov, and R. R. Schrock, Catalytic Reduction of Dinitrogen to Ammonia at a Single Molybdenum Center, Science Vol.301, pp.76-78 (2013).
 - 18) Y. Nishibayasi, Chemistry Vol.68, pp.37-42 (2013) [in Japanese].
 - 19) T. Haruyama, T. Namise, N. Shimoshimizu, S. Uemura, Y. Takatsuji, M. Hino, R. Yamasaki, T. Kamachi, and M. Kohno, Non-catalyzed one-step synthesis of ammonia from atmospheric air and water, Green Chemistry Vol.18, pp.4536-4541 (2016).
 - 20) A. Schutze, J. Y. Jeong, S. E. Babayan, P. Jaeyoung, G. S. Selwyn, and R. F. Hicks, The Atmospheric-pressure Plasma Jet: A Review and Comparison to Other Plasma Sources, IEEE Transactions on Plasma Science Vol.26, pp.1685-1694 (1998).
 - 21) K. Kitano and S. Hamaguchi, Low frequency atmospheric-micro-plasma jet, Oyo Buturi Vol.77, pp.383-389 (2008) [in Japanese].
 - 22) H. Kuwahata, T. Haraki, and I. Mikami, Superhydrophilization of Si Surface by Atmospheric-pressure Plasma Jet Irradiation: Analysis by Time-of-flight Secondary Ion Mass Spectrometry (TOF-SIMS), e-Journal of Surface Science and Nanotechnology Vol.11, pp.36-39 (2013).
 - 23) H. Kuwahata and T. Yamaguchi, Removal of Aluminum on Glass Substrate by Atmospheric-pressure Plasma Jet Irradiation, e-Journal of Surface Science and Nanotechnology Vol.14, pp.231-236 (2016).
 - 24) H. Kuwahata, Y. Murata, N. Hashimoto, and R. Segawa, Superhydrophilization of Surface of Aluminum Thin Film by Atmospheric-pressure Plasma Jet Irradiation, e-Journal of Surface Science and Nanotechnology Vol.16, pp.27-35 (2018).
 - 25) W. F. L. M. Hoeben, E. M. V. Veldhuizen, W. R. Rutgers, and G. M. W. Kroesen, Gas phase corona discharges for oxidation of phenol in an aqueous solution, Journal of Physics D: Applied Physics Vol.32, p.L133 (1999).
 - 26) T. Kuroki, K. Yoshida, H. Watanabe, M. Okubo, and T. Yamamoto, Decomposition of Trace Phenol in Solution Using Gas-Liquid Interface Discharge, Japanese Journal of Applied Physics Vol.45, pp.4296-4300 (2006).
 - 27) S. Ikawa, K. Kitano, and S. Hamaguchi, Effects of pH on Bacterial Inactivation in Aqueous Solutions due to Low-temperature Atmospheric Pressure Plasma Application, Plasma Processes and Polymers Vol.7, pp.33-42 (2010).
 - 28) H. Kuwahata, T. Yamaguchi, R. Ohyama, and A. Ito, Inactivation of *Escherichia coli* using atmospheric-pressure plasma jet, Japanese Journal of Applied Physics Vol.54, p.01AG08 (2015).
 - 29) G. Fridman, G. Friedman, A. Gutsol, A. B. Shekhter, V. N. Vasilets, A. Fridman, Applied Plasma Medicine. Plasma Processes and Polymers Vol.5, pp.503-533 (2008).
 - 30) M. G. Kong, G. Kroesen, G. Morfill, T. Nosenko, T. Shimizu, J. V. Dijk, J. L. Zimmermann, Plasma medicine: an introductory review, New Journal of Physics Vol.11, p.115012 (2009).
 - 31) G. Fridman, A. Shereshevsky, M. M. Jost, A. D. Brooks, A. Fridman, A. Gutsol, V. Vasilets, and G. Friedman, Floating Electrode Dielectric Barrier Discharge Plasma in Air Promoting Apoptotic Behavior in Melanoma Skin Cancer Cell Lines, Plasma Chemistry and Plasma Processing Vol.27, pp.163-176 (2007).
 - 32) S. Iseki, K. Nakamura, M. Hayashi, H. Tanaka, H. Kondo, H. Kajiyama, H. Kano, F. Kikkawa, and M. Hori, Selective killing of ovarian cancer cells through induction of apoptosis by nonequilibrium atmospheric pressure plasma. Applied Physics Letters Vol.100, p.113702 (2012).
 - 33) Y. Ogawa, N. Morikawa, A. Ohkubo-Suzuki, S. Miyoshi, H. Awakawa, Y. Kita, and S. Nishimura, An Epoch-Making Application of Discharge Plasma Phenomenon to Gene-transfer. Biotechnology and Bioengineering Vol.92, pp.865-870 (2005).
 - 34) M. Leduc, D. Guay, R. L. Leask, and S. Coulombe, Cell permeabilization using a non-thermal plasma. New Journal of Physics Vol.11, pp.115021 (2009).
 - 35) H. Kuwahata, K. Kimura, and R. Ohyama, Decolorization of Methylene Blue Aqueous Solution by Atmospheric-pressure Plasma Jet, e-Journal of Surface Science and Nanotechnology Vol.8, pp.381-383 (2010).
 - 36) T. Inoue, T. Tsugane, Y. Oda, and H. Kuwahata, Decolorization of tar dye aqueous solution by atmospheric-pressure plasma jet, Journal of Advanced Science Vol.30, p.30107 (2018) [in Japanese].
 - 37) H. Kuwahata, D. Sato, Y. Kezuka, Y. Oda, Decolorization of Amaranth aqueous solution by atmospheric-pressure plasma jet irradiation, Japanese Journal of Applied Physics Vol.59, p.SAAB06 (2020).
 - 38) H. Kuwahata and I. Mikami, Generation of H₂O₂ in Distilled Water Irradiated with Atmospheric-pressure Plasma Jet, e-Journal of Surface Science and Nanotechnology Vol.11, pp.113-115 (2013).
 - 39) H. Kuwahata and I. Mikami, High Performance Liquid Chromatography Analysis of Distilled Water Irradiated with Atmospheric-pressure Plasma Jet, Proceedings of the School of Engineering Tokai University, Series E Vol.40, pp.1-6 (2015).
 - 40) K. Kimura, I. Mikami, and H. Kuwahata, Generation of nitrate ions in distilled water irradiated with atmospheric-pressure plasma jet, Proceedings of the School of Engineering Tokai University, Series J Vol.52, pp.9-14 (2012) [in Japanese].
 - 41) H. Kuwahata and I. Mikami, Generation of Nitric Acid and Nitrous Acid in Distilled Water Irradiated with Atmospheric-pressure Plasma Jet, e-Journal of Surface Science and Nanotechnology Vol.12, pp.410-413 (2014).
 - 42) D. Braun, U. Kuchler, and G. Pietsch, Behaviour of NO_x in air-fed ozonizers, Pure and Applied Chemistry Vol.60, pp.741-746 (1988).
 - 43) J. S. Chang, P. A. Lawless, and T. Yamamoto, Corona Discharge Processes, IEEE Transactions on Plasma Science Vol.19, pp.1152-1166 (1991).
 - 44) J. Winter, H. Tresp, M. U. Hammer, S. Iseni, S. Kupsch, A. Schmidt-Bleker, K. Wende, M. D'unnbier, K. Masur,

- K. D. Weltmann, and S. Reuter, Tracking plasma generated H_2O_2 from gas into liquid phase and revealing its dominant impact on human skin cells, *Journal of Physics D: Applied Physics* Vol.47, p.285401 (2014).
- 45) N. Srivastava and C. Wang, Effect of N_2 and O_2 on OH radical production in an atmospheric helium microwave plasma jet, *Plasma Science Technology* Vol.21, p.115401 (2019).
- 46) Y. R. Luo, *Comprehensive Handbook of Chemical Bond Energies* (CRC Press Boca Raton, Florida, 2007).
- 47) V. I. Vedeneyev, L. V. Gurvich, V. N. Kondrat'yev, V. A. Medvedev, and Y. L. Frankevich, *Bond Energies, Ionization Potentials and Electron Affinities* (St. Martin's Press, New York, 1962).
- 48) Y. Hayashi, S. Hirao, Y. Zhang, and T. Gans, Argon metastable state densities in inductively coupled plasma in mixtures of Ar and O_2 , *Journal of Physics D: Applied Physics* Vol.42, p.145206 (2009).
- 49) A. R. Hoskinson, J. Gregorio, J. Hopwood, K. Galbally-Kinney, S. J. Davis, and W. T. Rawlins, Argon metastable production in argon-helium microplasma, *Journal of Applied Physics* Vol.119, p.233301 (2016).

Basic Study on Hybrid Systems to Improve the Vehicle Performance of Small Race Car (Investigation of Gear Ratios for Hybrid Systems Using Lap Time Simulation)

by

Ikkei KOBAYASHI^{*1}, Kazuki OGAWA^{*2}, Daigo UCHINO^{*2}, Keigo IKEDA^{*2}, Taro KATO^{*2},
Ayato ENDO^{*3}, Takayoshi NARITA^{*4}, Hideaki KATO^{*4} and Hiroyuki MORIYAMA^{*5}

(Received on Mar. 31, 2022 and accepted on Jul. 7, 2022)

Abstract

To improve the dynamic performance of small hybrid racing vehicles which use an electric motor and internal combustion engine, we propose a hybrid system to synchronize these torques with a simple configuration. The proposed hybrid system is suitable for a small race car: it is lightweight and can be arranged in various layouts with a simple structure using chains and sprockets. To investigate the control system for the hybrid system, it is necessary to analyze the dynamic performance of a vehicle in which the proposed system is installed. Therefore, we constructed a dynamic simulation when the vehicle was driven on a circuit. This paper investigates the motor gear ratio and final gear ratio for optimizing the vehicle performance of the hybrid system in a small race car using lap time simulation. The analysis results show that not only can the optimum setting be obtained by changing the final reduction ratio and the reduction ratio of the motor in the circuit, but also that the optimum value varies with different speed ranges in different circuits.

Keywords: Hybrid vehicles, Torque synthesizer, Small race car, Vehicle dynamics, Lap time simulation

1. Introduction

To examine the performance of a vehicle, three aspects of performance are evaluated: acceleration, turning, and braking. In recent years, race car, which pursue vehicle performance to the extreme, have begun to use hybrid systems consisting of an internal combustion engine and an electric motor as a power source. Hybrid vehicles, which are powered by two systems, an internal combustion engine and a motor, use the characteristics of the motor to compensate for the lack of torque in the low-speed range of gasoline-powered vehicles, and can be expected to deliver high torque and high acceleration over a wide speed range. Taking advantage of these advantages, recent general vehicles equipped with hybrid systems on the market aim to reduce fuel consumption by downsizing the internal combustion engine. Research on hybrid systems for energy management and comfortable

driving with a primary focus on improving fuel economy has been actively conducted^{1,2)}. In race cars, on the other hand, the most important objective is to win the competition. To achieve this objective, it is of utmost importance to improve the dynamic performance of the powertrain, which consists of the engine and electric motor, and to minimize the lap time. In order to drive faster on a defined circuit, the acceleration performance must be improved, especially to reach the maximum speed in a short time. In previous studies, battery optimal control methods for hybrid systems and comparison of acceleration performance for different layouts of two power systems have been reported to minimize lap time^{3,4)}, but there have not been enough studies to examine more active use of hybrid systems for driving performance. In addition, these studies have been performed on hybrid systems such as conventional series, parallel, power-split, and series-parallel hybrid powertrains⁵⁾. These systems use gears or planetary gears to combine the power of the engine and electric motor⁶⁾, but have drawbacks such as heavy systems and limited parts layout. Therefore, the authors have proposed a hybrid system suitable for small race car, which is lightweight and can be arranged in various layouts with a simple structure using chains and sprockets, and have studied the improvement of dynamic performance of vehicles by hybrid systems⁷⁾. Lap time simulation is used to predict vehicle performance in a

*1 Graduate Student, Course of Mechanical Engineering

*2 Graduate Student, Course of Science and Technology

*3 Assistant Professor, Hokkaido University of Science

*3 Research Associate, Tokyo University of Technology

*3 Assistant Professor, Fukuoka Institute of Technology

*4 Junior Associate Professor, Department of Prime Mover Engineering

*5 Professor, Department of Prime Mover Engineering

given circuit. This is a tool that converts various elements of a vehicle into lap times. There are many types of simulation methods, ranging from simple steady-state simulations to multi-body simulations involving complex transient phenomena⁸⁻¹¹). Previous studies have reported the usefulness of quasi-steady-state simulations in terms of computational load and time prediction accuracy^{12,13}). The nonlinear tire model¹⁴) and the four-wheels model¹⁵) that considers load transfer have also been applied to the tire characteristics. However, these studies were conducted on vehicles powered only by engines, and there is no sufficient study of the effect of the output characteristics of the hybrid system proposed by the authors on the reduction of running time in a circuit consisting of multiple straight lines and corners with varithesizingous curvatures. Therefore, we used a quasi-steady-state method with a small computational load and high prediction accuracy to calculate the lap time in a given circuit, and studied the dynamic performance of the hybrid system. In this report, the effects of changing the motor gear ratio and final gear ratio of a rear-wheel-drive parallel hybrid system on driving performance were investigated using a simple vehicle model that does not consider nonlinear tire models or load transfer as a basic study and a calculation method for quasi-steady-state lap time simulation.

The novelty of this paper is the establishment of a simulation of the dynamic performance of a vehicle with motor assist for the torque of the engine shifted by the transmission. In many competition vehicles equipped with such hybrid systems, a motorcycle engine with a transmission built into the engine case is used. Few reports have been published on hybrid systems in which an electric motor assists the torque already reduced by the transmission at the engine output shaft. This paper describes a lap performance simulation of such a hybrid system and the calculation of optimal parameters for a given circuit as an actual situation.

2. Hybrid Systems for Small Race Car

As the subject of the hybrid system to be installed in the small race car, we referred to Formula Hybrid, the hybrid division of Formula SAE, which is developed worldwide as an educational program for students who want to become automotive engineers, and used the regulations of this competition.

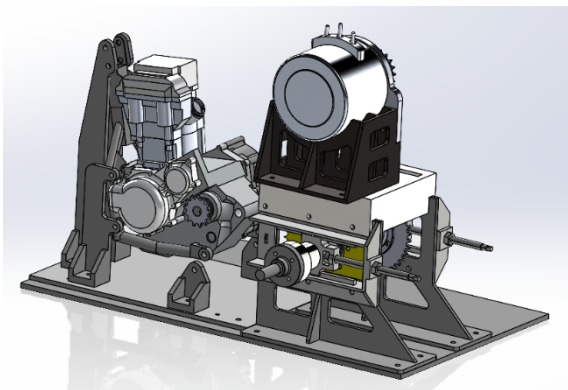


Fig. 1 3D model of the hybrid system.

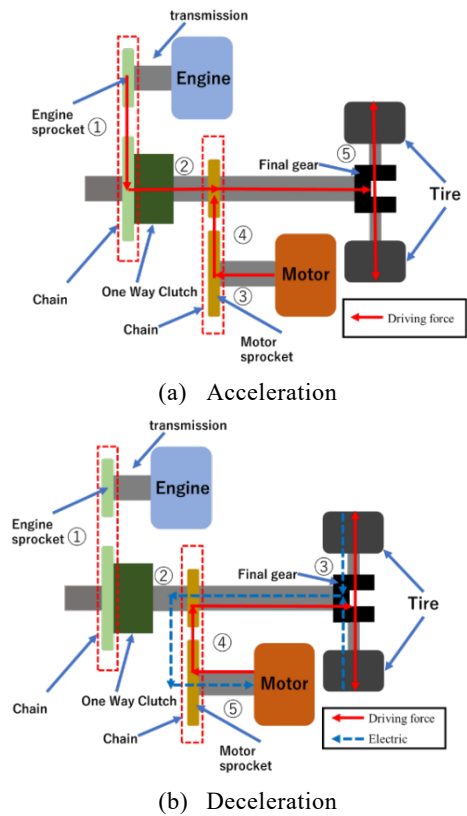


Fig. 2 Proposal of a device for synthesizing traction force generated by internal combustion engine and electric motor.

2.1 Structure of the hybrid system

The hybrid system is equipped with a torque synthesizer instead of the planetary gear transmission used in many passenger cars. Figure 1 show 3D model of the proposed hybrid system.

The planetary gear type has many layout restrictions and is difficult to maintain, whereas the torque synthesizer has the advantage of easy maintenance, fewer design requirements on the chassis side, and the ability to use a chain, making it easy to layout. This makes it suitable for hybridization of motorcycle engines.



Fig. 3 Internal combustion engine YAMAHA G363E.

Table 1 Specifications of the engine.

Engine Model Number	G363E
Engine Type	250 cc liquid-cooled DOHC 4-stroke; 4 valves
Bore × Stroke	77.0 mm × 53.6 mm
Compression Ratio	11.8:1
Fuel Delivery	Fuel injection
Ignition	TCI: Transistor Controlled Ignition
Transmission	Constant-mesh 6-speed, multiplate wet clutch
Max Power	23 kW(35 PS)/10000 rpm
Max Torque	24 N · m(2.2 kg · m)/8000 rpm

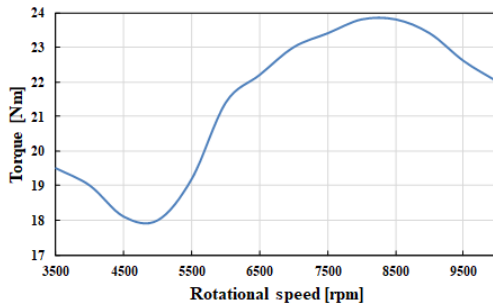


Fig. 4 Relationship between engine rotational speed and torque.

Figure 2 shows schematic diagram of proposed hybrid system. As shown in Fig. 2(a), in the proposed hybrid system, during acceleration, the shaft torque generated by the engine is shifted through the transmission, decelerated and transmitted from the engine sprocket to the drive shaft side sprocket by a chain, and then transmitted to the axle shaft through the one-way clutch and final gear. The shaft torque generated by the motor is decelerated and transmitted to the drive shaft side sprocket by a chain, and then transmitted to the axle by the final gear. The drive torque generated around the tire is the sum of the above two torques transmitted to the axle shafts

On the other hand, during deceleration, as shown in Fig. 2(b), there is no drive power from the engine and the motor drive power is not transmitted to the engine via the one-way clutch, and the engine sprocket on the drive shaft side idles. In



Fig. 5 Electric motor Moterenergy ME0913.

Table 2 Specifications of the motor.

Drive voltage	DC24 V - 96 V
Maximum current	550 A
Maximum rotation speed	5000 rpm (No load)
Maximum output	30 kw (DC 96 V)
Maximum torque	90 Nm
Continuous output	12 kw (DC 96 V)
Continuous current	180 A
Continuous efficiency	92%
Continuous rotation speed	3000 rpm
Weight	15.9 kg
Poles	4 (Magnet 8)
Cooling method	Air cooling Forced fan system

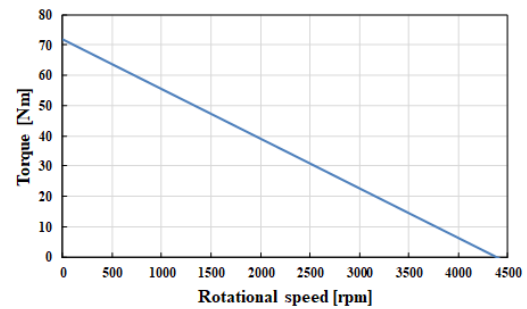


Fig. 6 Relationship between motor rotational speed and torque.

addition, the braking force on the tire contact patch generates torque on the axle shaft in the opposite direction of acceleration, which is transmitted to the motor shaft by the final gear and sprockets. These torques can generate power to the motor and regenerate energy.

2.2 Two power sources in a hybrid system

The internal combustion engine in the hybrid system is the G363E used in the YAMAHA WR250R shown in Fig. 3. Table 1 shows the specifications of the engine, and Fig. 4 shows the two-dimensional data of relationship between rotational speed and torque.

The electric motor in the hybrid system is specified to have a maximum output of less than 30 kW and uses the air-cooled Motenergy ME0913 brushless motor shown in Fig. 5. Table 2 shows the specifications of the motor, and Fig. 6 shows the relationship between rotational speed and torque.

The torque relative to the rotational speed of these two power sources is synthesized using the values of the respective gear ratios in the engine, the engine and motor gear ratios up to the drive shaft, and the final gear ratio from the drive shaft to the axle shafts.

3. Calculation Method of Quasi-Steady-State Lap Time Simulation

In this simulation, the vehicle is always assumed to be in equilibrium and yaw motion is ignored. The velocity in each section is determined as the maximum velocity that can be achieved when driving within the range of a three-dimensional map consisting of lateral acceleration, longitudinal

acceleration, and speed, called the GGV vehicle performance envelope, which is pre-calculated from the vehicle model. Figure 7 shows a schematic of the GGV vehicle performance envelope. It can be read that the performance of longitudinal acceleration and lateral acceleration increases or decreases depending on the size of the velocity. In general, changes in velocity affect the vehicle's friction ellipse due to aerodynamics and engine speed. Lap time is calculated by discretizing the times for each segment and summing the times for all segments.

3.1 Simplified vehicle model

The lateral and longitudinal forces $F_{x,y}$ at the tire contact patch are calculated from the simplified linear tire model shown in eq. (1) by multiplying the vertical load F_z by the friction coefficients in the lateral and longitudinal directions $\mu_{x,y}$.

The vertical load is the weight produced by the vehicle mass m and the acceleration of gravity g and the aerodynamic function downforce L , which is calculated by eq. (2). The downforce is then calculated in eq. (3) and is found to be a function of speed v .

$$F_{x,y} = F_z \cdot \mu_{x,y} \quad (1)$$

$$F_z = mg + L \quad (2)$$

$$L = 0.5 \cdot C_L A \rho v^2 \quad (3)$$

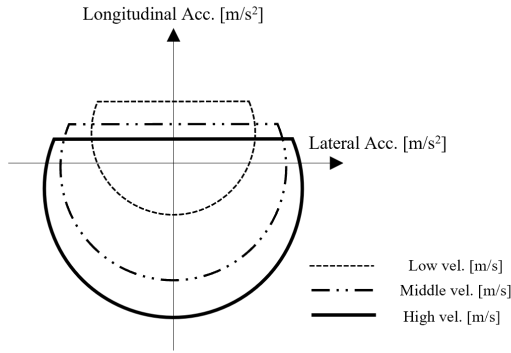


Fig. 7 Schematic of the GGV vehicle performance envelope.

The tractive force F_t derived from the hybrid powertrain system is calculated from the vehicle speed v , each gear ratio gr , and tire radius r_t using eq. (4) to calculate the engine speed and motor speed ω , respectively, and the shaft torque T of the two systems from these rotational speeds are added together and calculated by eq. (5) using the tire radius.

$$\omega = \frac{v \cdot gr}{r_t} \quad (4)$$

$$F_t = \frac{T \cdot gr}{r_t} \quad (5)$$

The lower of the tire longitudinal force and the powertrain-derived driving force obtained in eqs. (1) and (5) is used as the longitudinal force at the vehicle center of gravity. This is because the longitudinal force at the tire contact patch is highly dependent on the slip ratio, which is the ratio of the vehicle speed to the rotational speed of the tire, and the drive torque generates the tire rotational speed, which varies only slightly, around 0 - 0.2, hence the approximation in eq. (6) is used. Longitudinal forces at the vehicle center of gravity can be calculated by allowing the drag force D of the aerodynamic function to be taken into account. Drag force is a function of speed, as is downforce in eq. (3), and can be calculated in eq. (7) using the drag coefficient C_L .

$$T \approx F_x \cdot r_t \quad (6)$$

$$D = 0.5 \cdot C_D A \rho v^2 \quad (7)$$

With the calculations up to this point, it is possible to calculate the maximum lateral and longitudinal forces for each velocity. In order to calculate the combined state in which these longitudinal and lateral forces occur simultaneously in the quasi-steady-state, the friction ellipse assumption in eq. (8) is made to simplify the problem.

$$(\mu_{x,y} \cdot F_z)^2 = F_x^2 + F_y^2 \quad (8)$$

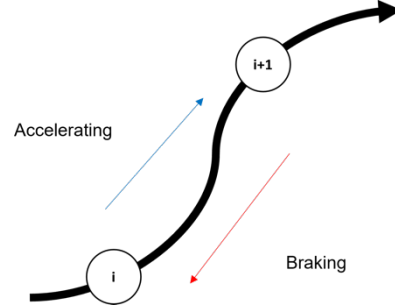


Fig. 8 Illustration of quasi-steady-state simulation.

3.2 Calculation method for lap time in quasi-steady-state

Quasi-steady-state lap time simulation in this research is calculated from pre-discretized circuit data of radius of curvature and distance. These can be obtained from GPS and data logging systems installed in the actual vehicles.

First, a critical speed profile is created in eq. (9) using the corner radius R and the maximum lateral acceleration a_y calculated from the vehicle model. At this time, the velocity within each section is not within the GGV vehicle performance envelope when longitudinal acceleration occurs due to the maximum lateral acceleration. To solve this problem, the critical speed profile is used to calculate the longitudinal acceleration a_x of the velocity v within the adjacent section distance dx from the beginning and end of the circuit using eq. (10), and the acceleration and deceleration velocities are calculated by decreasing the velocity until it falls within the GGV vehicle performance envelope. An illustration of the

calculation of acceleration side velocity and deceleration side velocity within an adjacent section is shown in Fig. 8.

$$a_y = \ddot{y} = \frac{v^2}{R} \tag{9}$$

$$\left. \begin{aligned} dv &= v_i - v_{i-1} \\ dt &= \frac{dx}{v_i} \\ a_x &= \ddot{x} = \frac{dv}{dt} \end{aligned} \right\} \tag{10}$$

From these calculations, the intersection of the two velocities, the acceleration side velocity and the deceleration side velocity with respect to distance, is calculated as the braking start point, and the limit performance of the vehicle in the quasi-steady-state can be predicted.

The computation run time is very fast; a single lap simulation takes less than 30 seconds. This makes it possible to analyze the sensitivity of the lap times when various parameters are changed.

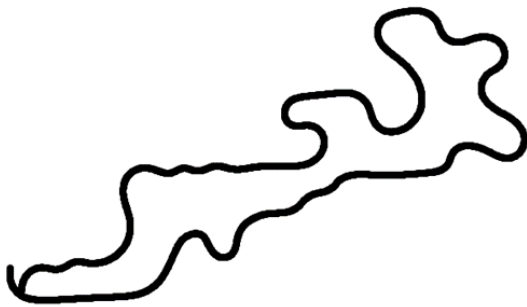


Fig. 9 Schematic of evaluation 900-meter circuit.

Table 3 Vehicle basic parameters.

General Data		Engine Data	
Vehicle Type	FSAE	Thermal Efficiency [%]	35
Mass [kg]	369.7	Transmission Data	
Driven Type	2WD	Gear1	2.642
Aero Data		Gear2	1.812
Drag Coefficient	0.8	Gear3	1.318
Downforce Coefficient	1.2	Gear4	1.04
Front Area [m ²]	1.1	Gear5	0.888
Air Density [kg/m ³]	1.226	Gear6	0.785
Tire Data		Final Drive Ratio	3.145
Tire Radius [m]	0.128	Drive Efficiency [%]	83
Rolling Resistance	0.03		
Longitudinal Friction	1.4		
Lateral Friction	1.5		

4. Final Gear Ratio and Motor Reduction Gear Ratio Study Using Lap Time Simulation

4.1 Simulation Calculation Conditions

In order to evaluate the vehicle performance of the proposed small race car, the power supply voltage of the electric motor is 77 V, based on the Table 2. A reduction

gearbox was added to the motor, the engine and motor speeds were individualised, a program was created to allow the torque and speed of the motor to be varied, and the reduction ratio of the motor and final gear ratio were changed for lap time simulations.

The primary reduction ratio of the engine was set to 3.12, and no lower than 3500 rpm was used in this study because the engine would stop at low engine speeds when starting the vehicle. Therefore, the initial speed at start-up was set in first gear and at an engine speed of 3500 rpm. The engine speed is shifted up when the engine speed reaches 10000 rpm, and the value at 6th gear and 10000 rpm is held constant in the simulation after 6th gear and 10000 rpm. The engine and

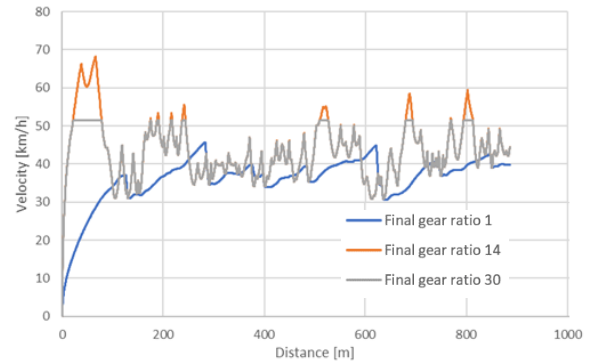


Fig. 10 Relationship between distance and vehicle velocity for each final gear ratio.

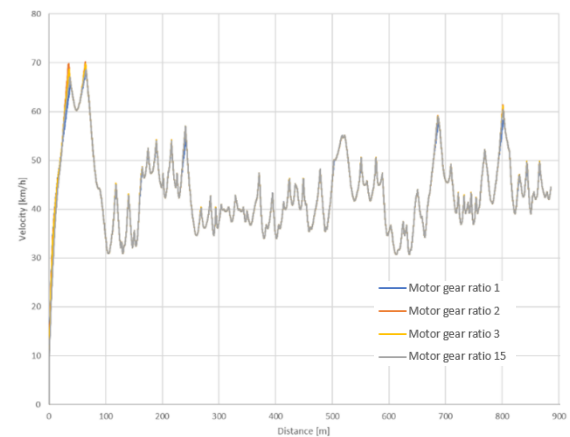


Fig. 11 Relationship between distance and vehicle velocity for each electric motor reduction gear ratio.

motor shaft torques were modeled by polynomial approximation using the two-dimensional data in Fig. 4 and 6. For the other basic parameters, the simplified vehicle model in Table 3 was used. The evaluation circuit was a 900 m closed circuit with a series of left and right turns, as shown in Fig. 9. These are the circuits used for Endurance Event in Formula

SAE Japan¹⁶⁾ which is based on FORMULA SAE Rules 2022¹⁷⁾ defined by Society of Automotive Engineers International, a project similar to the vehicle proposed in this study.

4.2 Analysis Result

Simulations were carried out on the small hybrid race car with varying final and motor reduction gear ratios. We aimed to minimize the lap time in order to validate the effective vehicle state for the purpose of predicting the scale of the vehicle state to be achieved on the course in order to construct a multi-input, multi-output control algorithm to be installed in the proposed vehicle. The objective is to minimise lap times and the role of the powertrain is to achieve the maximum possible acceleration in each velocity range. There is a trade-off between lowering the final gear ratio, which reduces the

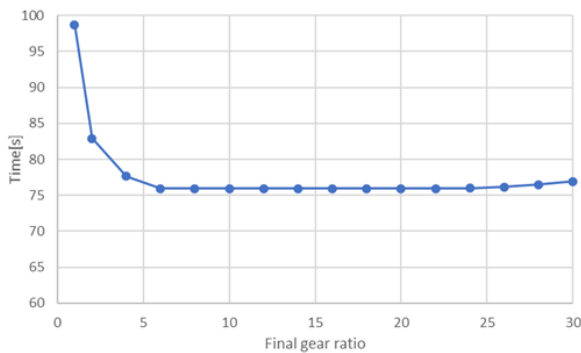


Fig. 12 Relationship between final gear ratio and lap time.

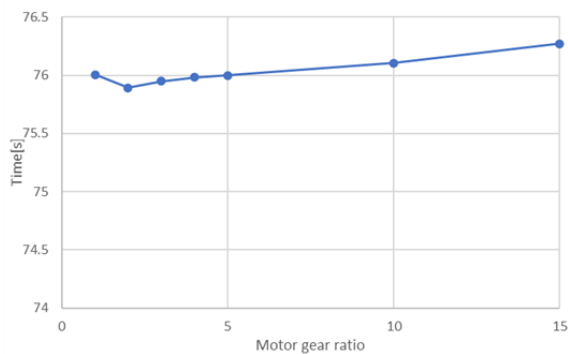


Fig. 13 Relationship between electric motor reduction gear ratio and lap time.

acceleration that can be generated due to the reduction in axle torque, and raising it too high, which reduces the maximum speed due to power unit speed limitations, and the tyres reaching their slip limit, resulting in excess powertrain dynamic performance. Figure 10 shows analyzed results in final gear ratio 1, 14, 30. This figure shows that when the final gear ratio is 1, the overall slope of speed is low, and when the final gear ratio is 30, the speed has hit its head. In addition, the slope of the speed is always the same when comparing final gear ratios 14 and 30, indicating that an excessive gear ratio exceeds the limit of the longitudinal force of the tyres, resulting in a wasteful use of powertrain dynamic performance.

The reduction ratio of the motor has a smaller range of gear ratio settings, as the motor can generate more torque at

lower speeds due to the characteristics of the motor. The analyzed relationship between distance and velocity for each reduction ratio of the motor is shown in Fig. 11. The speed range where the characteristics of the motor can be utilised is the high velocity range, and the difference between each gear ratio appears at the point where the highest velocity is reached in one lap. Extremely large motor gear ratios exceed the limits of the longitudinal force of the tyres, and the advantages of the hybrid system disappear.

The relationship between final gear ratio and obtained lap time is shown in Fig. 12, and the relationship between motor reduction gear ratio and running time is shown in Fig. 13. The simulations on this evaluation circuit produced the fastest results when the final gear ratio was 14 and the motor reduction gear ratio was 2.

5. Conclusion

This paper presents a fundamental study of the motor gear ratio and final gear ratio for optimizing the vehicle performance of the proposed hybrid system in a small race car, using a simulation-based approach. Specifically, as a first step to predict the scale of the vehicle state to be achieved on the course, such as the speed of the vehicle to construct a multi-input multi-output control algorithm for the proposed racing car, we found the optimal solution of the drive gear ratio for the racing car to predict the effective vehicle state for the competition.

Within the report, the superiority of the hybrid system using the torque synthesizer mechanism was asserted in comparison with the planetary gear mechanism, and the modeling method along this mechanism was briefly presented. And, the theory and utility of quasi-steady state lap time simulation, which models the vehicle and predicts its performance in a simplified manner, as a powerful tool to help optimize powertrain systems, is presented. By extending the model, more practical simulations can be expected, and parameter sensitivity analysis can be performed outside of this research.

In the future, based on the analysis results, we will proceed with the development and design of the actual vehicle, as well as simulation of closed-loop circuit driving. We will also develop a vehicle dynamics simulation tool that includes more detailed nonlinear elements in order to predict complex vehicle motion phenomena that occur when the vehicle is actually driven and to build control algorithms.

References

- 1) L. V. Perez and A. Pilotta: Optimal power split in a hybrid electric vehicle using direct transcription of an optimal control problem, *Mathematics and Computers in Simulation*, Vol.79, pp.1959-1970 (2004).
- 2) A. Viehmann and S. Rinderknecht: Investigation of the Driving Comfort of the DE-REX Powertrain based on Vehicle Measurements, *International Federation of Automatic Control Papers Online*, Vol.52-15, pp.103-108 (2019).

- 3) R. Lot and S. Evangelou: Lap Time Optimization of a Sports Hybrid Electric Vehicle, Proceedings of the World Congress on Engineering, Vol.3, pp.1711-1716 (2013).
- 4) S. Lambert, S. Maggs, P. Faithfull, and A. Vinsome: DEVELOPMENT OF A HYBRID ELECTRIC RACING CAR, Hybrid and Eco-Friendly Vehicle Conference, IET HEVC, Dec., pp.1-5 (2008).
- 5) G. Wu, X. Zhang, and Z. Dong: Powertrain architectures of electrified vehicles: Review, classification and comparison, Journal of the Franklin Institute, Vol.352, pp.425-448 (2015).
- 6) M. Mohammadpour and H. Rahnejat: Dynamics and efficiency of planetary gear sets for hybrid powertrains, Proceedings of the Institution of Mechanical Engineers, Part C: Journal of Mechanical Engineering Science, Vol. 230, pp.1359-1368 (2015).
- 7) Y. Sato, T. Narita, H. Kato and T. Okamoto: Proposal of Power Synthesis Mechanism in Hybrid System for Compact Racing Car: A Fundamental Consideration on Structural Design and Vehicle Movement Performance, Proceedings School of Engineering Tokai Univ., Series E, Vol.43, pp.31-37 (2018).
- 8) W. F. Milliken, D. L. Milliken, *Race Car Vehicle Dynamics*, Society of Automotive Engineers, Inc., Warrendale, p.343 (1995).
- 9) D. Casanova, R. S. Sharp, and P. Symons: Minimum Time Manoeuvring: The Significance of Yaw Inertia, Vehicle System Dynamics, Vol.34, pp.77-115 (2000).
- 10) N. D. Bianco, R. Lot and M. Gadola: Minimum time optimal control simulation of a GP2 race car, Proceedings of the Institution of Mechanical Engineers, Part D: journal of Automobile Engineering, Vol.232, pp.1180-1195 (2017).
- 11) C. Patton: Development of Vehicle Dynamics Tools for Motorsports, Doctor of Philosophy dissertation, Oregon State University, pp.61-91 (2013).
- 12) D. L. Brayshaw and M. F. Harrison: A quasi steady state approach to race car lap simulation in order to understand the effects of racing line and centre of gravity location, Proceedings of the Institution of Mechanical Engineers, Part D: journal of Automobile Engineering, Vol.219, pp.725-739 (2005).
- 13) B. Siegler, A. Deakin and D. Crolla: Lap Time Simulation: Comparison of Steady State, Quasi-Static and Transient Racing Cornering Strategies, SAE Technical Paper 2000-01-3563, p.361 (2000).
- 14) H. B. Pacejka, *Tire and Vehicle Dynamics Third Edition*, Elsevier Ltd., Oxford, pp.176-183 (2012).
- 15) S. van Koutrik: Optimal Control for Race Car Minimum Time Maneuvering, Master of Science Thesis, Delft University of Technology, pp.118-121 (2015).
- 16) Course of Endurance Event in Formula SAE Japan, https://www.jsae.or.jp/formula/jp/student_formula/docu/14th_endurance.pdf
- 17) *FORMULA SAE Rules 2022*, Society of Automotive Engineers International, p.132 (2022).

Numerical Analysis of the Propagation of Detonation Wave Plunging Entry of a Combustible Premixed Jet Train

by

Faming WANG^{*1}, Toshiharu MIZUKAKI^{*2} and Shingo MATSUYAMA^{*3}

(Received on Mar. 16, 2022 and accepted on Jul. 7, 2022)

Abstract

In the flow field of a rotating detonation engine (RDE), the detonation wave propagates through the reaction with the continuously injected fuel and oxidant mixture. In previous research using an actual RDE, due to insufficient mixing, combustion chamber shape, centrifugal force, etc., the detonation wave velocity generated in the RDE was usually significantly lower than the characteristic Chapman-Jouguet(C-J) velocity for the corresponding mixture. In this paper, to clarify the effect of detonation propagation by incomplete fuel mixing in the RDE, a linear detonation channel that simulates the RDE flow field was constructed and a numerical analysis of the propagation of detonation wave plunging entry of a combustible premixed jet train composed of ethylene(C_2H_4) and oxygen(O_2) was carried out. The numerical analysis results show that when the fuel is fully mixed with the oxidant and ignited with high energy, as the mass flow rate increases, the detonation velocity increases and approaches 92% of the C-J velocity. Compared with the 70% C-J velocity of an RDE with non-premixed fuel, the improvement is significant.

Keywords: Detonation propagation, Rotating detonation engine, Turbulent-combustion, Numerical analysis

1. Introduction

In recent years, detonation engines have been favored by researchers because of their simple structure and high efficiency. Among them, the Rotating detonation engine (RDE) has the potential to completely replace the existing technology of traditional aerospace engines. In the future, it may become the main engine application in aviation, aerospace and other fields. At present, Russia, Poland, China, the United States, and other countries have carried out many RDE-related research and have made great progress. In Japan, The Japan Aerospace Exploration Agency (JAXA) also has great interest in Rotating Detonation Engine (RDE) and has begun basic research. Currently, RDE has been successfully run at JAXA Kakuda Space Center¹⁾.

Although there are many research results on RDE in various countries, propagation of the detonation wave inside the RDE has not been clearly revealed through experiments, because the propagation of the rotating detonation wave is affected by the injection pressure, the curvature of the combustion channel and the fuel-oxidant mixture ratio¹⁻⁴⁾. Usually, RDE uses a non-premixed fuel injection method for safety, that results in insufficient fuel mixing. The detonation velocity generated in the RDE is usually Significantly lower than the characteristic Chapman-Jouguet velocity of the corresponding mixture, Cause

the thrust to reach the expected value, RDE has not been practical yet.

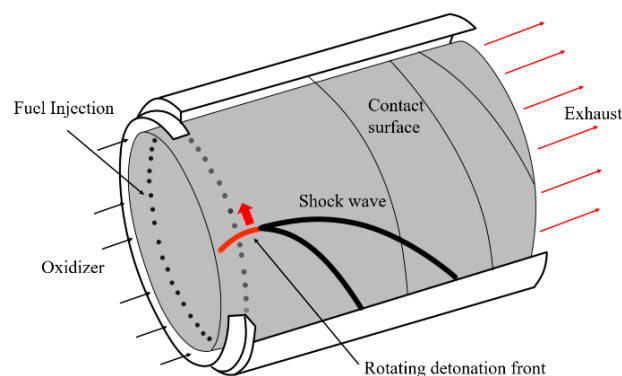


Fig. 1 Rotating Detonation Engine.

The objective of this study is to examine the reduction in the propagation velocity of detonation waves caused by partially mixed fuel. The method is to expand the annular combustion chamber of the RDE into a linear combustion chamber to eliminate the influence of shape and centrifugal force on the propagation of detonation, so that can investigate the influence of fuel on the propagation of detonation waves in detail. To clarify the influence of incomplete fuel mixing on the propagation of detonation, it is first necessary to master the propagation mode of detonation wave in the completely mixed fuel. a high precision

*1 Graduate Student, Course of Science and Technology

*2 Professor, Department of Aeronautics and Astronautics

*3 Japan Aerospace Exploration Agency

LES of propagation of detonation wave plunging entry the combustible premixed jet train was performed by using a supercomputer system.

2. Linear Detonation Channel

The linear detonation channel facility is shown in Fig. 2. It's unfolded a curved RDE combustion chamber into a linear shape. The fuel and oxidant enter the tube through a small hole at the bottom with a controllable flow rate, and it's possible to change its ignition mode by changing some parts. Both sides are equipped with quartz windows for optical visualization.

The advantage of the linear detonation channel is that the propagation of the detonation wave inside the channel is not affected by the shape and centrifugal force, and the observation windows on both sides of the passage can perform more clearer optical visualization.

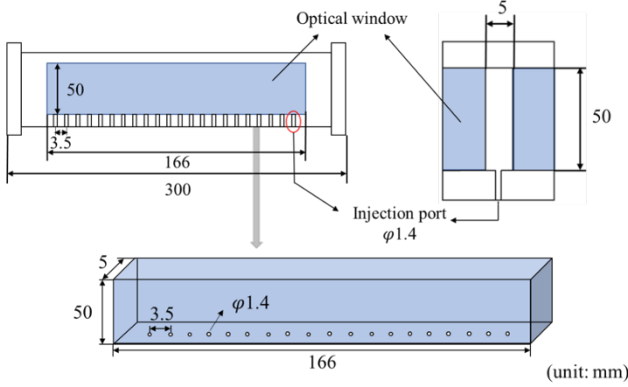


Fig. 2 Linear detonation channel.

As the injection condition of the envisioned experiment, a detonation tube filled with premixed ethylene oxygen having the same equivalent ratio as the experimental conditions is installed on the upstream side of the linear detonation channel. Detonation is generated by ignition, and the generated detonation wave enters the linear detonation channel.

3. Numerical Method

3.1 Numerical analysis code

In numerical analysis, we used JAXA's in-house code CHARIOT (Cost-effective High-order Accurate Reconstruction-scheme Intensively Optimized for Turbulent-combustion) that is designed for DNS/LES of turbulent combustion in aerospace propulsion systems⁵⁾. The governing equations of the flow used for the present LES analysis is compressible Navier-Stokes equation.

$$\frac{\partial \bar{\rho}}{\partial t} + \frac{\partial \bar{\rho} \bar{u}_i}{\partial x_i} = 0 \quad (1)$$

$$\frac{\partial \bar{\rho} \bar{u}_i}{\partial t} + \frac{\partial}{\partial x_j} \left\{ \bar{\rho} \bar{u}_i \bar{u}_j + \bar{p} \delta_{ij} - \bar{\tau}_{ij} + \bar{\rho} (\bar{u}_i \bar{u}_j - \bar{u}_i \bar{u}_j) \right\} = 0 \quad (2)$$

$$\frac{\partial \bar{\rho} \bar{e}}{\partial t} + \frac{\partial}{\partial x_i} \left\{ \bar{\rho} \bar{u}_i \bar{e} + \bar{\rho} \bar{u}_i + \bar{q}_i - \bar{u}_j \bar{\tau}_{ij} + \bar{\rho} (\bar{e} \bar{u}_i - \bar{e} \bar{u}_i) \right\} = 0 \quad (3)$$

$$\frac{\partial \bar{\rho} \bar{Y}_k}{\partial t} + \frac{\partial}{\partial x_i} \left\{ \bar{\rho} \bar{Y}_k \bar{u}_i - \bar{\rho} \bar{D}_k \frac{\partial \bar{Y}_k}{\partial x_i} + \bar{\rho} (\bar{Y}_k \bar{u}_i - \bar{Y}_k \bar{u}_i) \right\} = \bar{\omega}_k \quad (4)$$

LES analysis in this study is performed by implicit LES, in which all SGS terms are set to zero. For the detailed reaction model of ethylene combustion, 31 species 126 reactions model is used. In addition, operator-splitting method, and a Quasi-Steady-State approximation (QSS) are applied to reduce the stiffness associated with fast chemical reactions. The CHEMKIN database is used to calculate the thermodynamic and transport properties.

The governing equations are discretized by the finite volume method. The convective flux is calculated by SLAU2 scheme, and the viscous flux is obtained by the central difference method. High order spatial accuracy is realized by interpolating primitive variables (ρ , u , v , w , p , Y_s) at the cell interface. For the scalar variables (ρ , p , Y_s), the second-order MUSCL (Monotone Upwind Scheme for Conservation Laws) method is used, and the velocity components (u , v , w) are interpolated with a fifth order polynomial. In addition, to reduce the numerical dissipation in low velocity flow, the correction method by Thornber et al.⁶⁾ is applied to interpolated velocity components. For the time integration method, the three-stage Runge-Kutta method is employed.

Computation was carried out on the JAXA Supercomputer System (JSS3) installed at the Aeronautical Technology Directorate (ATD) of JAXA. Parallel computation was implemented by domain decomposition, with the Message Passing Interface (MPI) library used for inter-processor communication.

3.2 Numerical analysis model & injection conditions

The above device has two ignition modes by changing the components. Mode 1 is to insert a metal plate to make a long and narrow flow path to simulate actual RDE ignition, and Mode 2 is to directly ignite by connecting other detonation tubes. The two modes of the device and the corresponding calculation models are shown in Fig. 3. In the calculation model, the mark on the left is the ignition position, the black line is the solid wall, the red line is inflow boundary same as the fuel injection method of the device, and the yellow line is the outflow boundary. In the previous research of code validation, at a grid accuracy of 50 μm , the detonation propagation speeds duplicated the Chapman-Jouguet (CJ) velocity V_{CJ} well with very small errors less than several percent, and the error between the detonation pressure history of the numerical analysis results and the experimental value is within 10%⁷⁾⁸⁾. If the grid accuracy is increased, the triple point and cell structure will be clearer, but in the analysis of detonation engine, the influence of the cell is hardly so much on the propulsion performance⁹⁾. In this study, the detonation velocity is the main object of analysis, so it is appropriate that

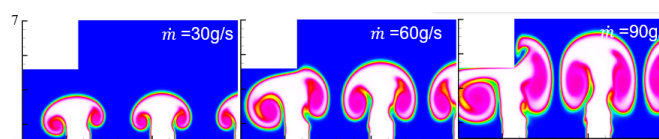


Fig. 5 Fuel injection height comparison at the same time.

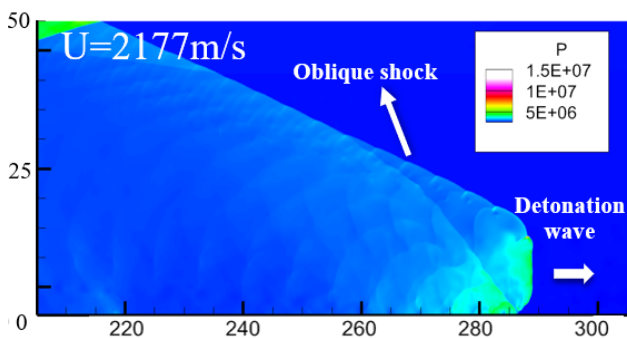


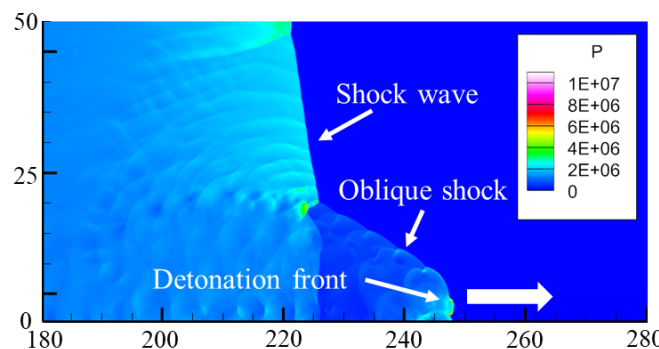
Fig. 6 Pressure distribution of $\dot{m} = 90$ g/s of ignition pressure 150 kPa.

4. Numerical analysis results of mode 2

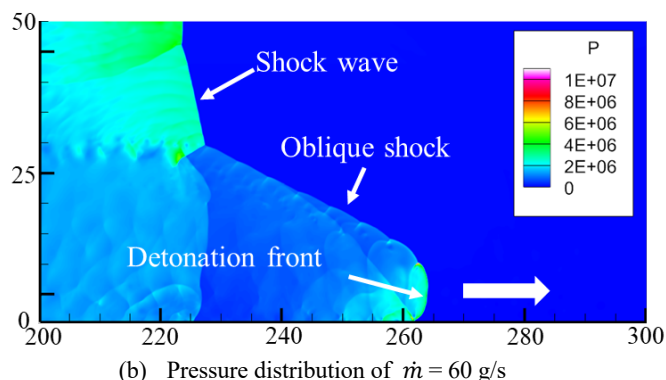
The numerical analysis results of Mode 2 are shown in Table 3 and Fig. 7. The detonation was successfully generated and propagated. With the increase of the mass flow rate, the detonation velocity gradually increased and reached about 92% of the theoretical value of C-J condition, which is a significant improvement compared with the non-premixed fuel which is usually lower than the theoretical value of 30%^(11,12).

Table 3 Detonation velocity results of mode 2.

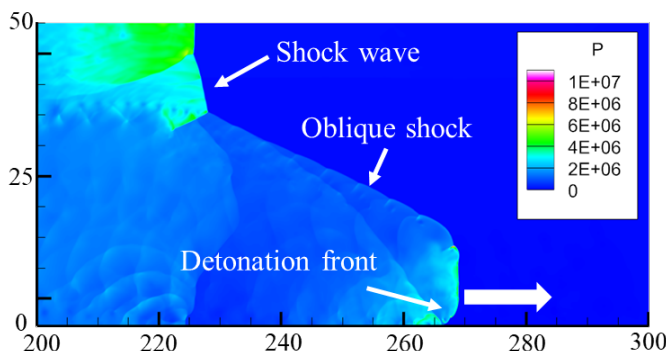
Mass flow rate	30 g/s	60 g/s	90 g/s
Detonation velocity	1725 m/s	1979 m/s	2266 m/s
C-J velocity	2439 m/s		



(a) Pressure distribution of $\dot{m} = 30$ g/s



(b) Pressure distribution of $\dot{m} = 60$ g/s



(c) Pressure distribution of $\dot{m} = 90$ g/s

Fig. 7 Numerical analysis results of mode 2.

5. Conclusions

Through the numerical analysis of the propagation of detonation wave plunging entry the combustible premixed jet train:

The ignition of the fuel in the combustion chamber and the formation of detonation propagation has a very high dependence on the ignition source energy. When the ignition energy is insufficient, the detonation did not occur or need a longer path to reach the expected value.

With the mass flow rate increases, the detonation velocity can gradually approach the C-J velocity, and reach more than 90% of the theoretical value. Compared with the traditional RDE using non-premixed fuel injection, where the detonation velocity is only about 70% of the theoretical value, the improvement is obvious. This shows that when the fuel is completely mixed, the propagation speed of detonation is greatly improved. If the existing RDE fuel injection method can be improved to make the fuel mixing more fully, the performance of the RDE can also be improved.

Acknowledgments

For this study, we used JAXA Supercomputer System generation 3 (JSS3).

References

- 1) M. Kojima et al.: Experimental Study of Rotating Detonation Rocket Engine at JAXA. Proceedings of The 32nd International Symposium on Shock Waves, OR-04-0120 (2019).
- 2) B. A. Rankin, D. R. Richardson, A. W. Caswell, A. G. Naples, J. L. Hokes and F. R. Schauer, *Combust. Flame* 176: pp.12-22 (2017).
- 3) C. Bedick, D. Ferguson and P. Strakey, *J. Prop. Pow.* Vol.35, No.4, pp.827-837 (2019).
- 4) J. Sun, S. Liu and Z. Lin: Numerical investigation of a rotating detonation engine under premixed/non-premixed conditions. *Acta Astronaut.* Vol.152, pp.630-638 (2018).
- 5) Shingo, M., Kazuya, I., Yoshio, N., Hideyuki, T., Toshiharu, M., Makoto, K., and Hideto, K: Large-Eddy Simulation of Rotating Detonation with a Non-premixed CH₄/O₂ Injection, AIAA 2020-1174 (2020) .
- 6) Thornber, B., Mosedale, D., Drikakis, D., Youngs, D., and Williams, R. J. R., "An Improved Reconstruction Method for Compressible Flows with Low Mach Number Features," *Journal of Computational Physics*, Vol.227, pp.4873–4894 (2008).
- 7) Faming, W., Toshiharu, M., Shingo, M. Visualization and CFD of the influence of mixing on detonation wave propagation inside a rotating-detonation engine by using linear detonation channel, AIAA 2022-1456 (2021).
- 8) Faming, W., Toshiharu, M., Shingo, M. NUMERICAL ANALYSIS OF DETONATION STRUCTURE BY USING CHARIOT. The 31st International Symposium on Transport Phenomena, p.153 (2020).
- 9) Nobuyuki, T., Koichi, A, K. Rotating Detonation Engines, *Journal of the Combustion Society of Japan*, Vol.55 No.174, pp.349-363 (2013).
- 10) Yungster. S, Radhakrishnan. K, and Perkins. H. D: Structure and Stability of One-Dimensional Detonations in Ethylene-Air Mixtures, AIAA Paper 2003-4248, E-14143 (2003).
- 11) Shingo, M: Development of Turbulent Combustion Analysis Code CHARIOT. Proceedings of The 49th JSASS Annual Meeting, 2C05 (2018).
- 12) Zhukov, V. P. and Kong, A. F: A compact reaction mechanism of methane oxidation at high pressures. *Progress in Reaction Kinetics and Mechanism*, Vol.43, No.1, pp.62–78 (2018).
- 13) Takayuki A., Keisuke Y, Youhi M, Nobuyuki T: and A. Koichi H., Numerical Analyses on Ethylene/Oxygen Detonation with Multistep Chemical Reaction, *Combustion Science and Technology*, Vol.188, No.3, pp.346-369 (2016).
- 14) Takuma, S, Stephen, V, Venkat, R: Detailed Chemical Kinetics based Simulation of Detonation-Containing Flows, Proceedings of ASME Turbo Expo 2018 Turbomachinery Technical Conference and Exposition (2018).
- 15) M. Kojima et al.: Thrust characteristics and detonation propagation behavior in Japan's largest RDRE. Symposium on Shock Waves in Japan, 2A2-1 (2020).
- 16) Shingo, M et al.: CFD Analysis on Combustion in a Rotating Detonation Combustor. Symposium on Shock Waves in Japan, 2A3-1 (2020).
- 17) Prakash, S., Fiévet, R., Raman, V., Burr, J., & Yu, K. H: Analysis of the detonation wave structure in a linearized rotating detonation engine. *AIAA Journal*, Vol.58, No.12, pp.5063–5077 (2019).
- 18) Burr, J. R., & Yu, K. H: Experimental characterization of RDE combustor flowfield using linear channel. Proceedings of the Combustion Institute, Vol.37, No.3, pp.3471–3478 (2019).

EDITORIAL COMMITTEE OF PROCEEDINGS OF
THE SCHOOL OF ENGINEERING OF
TOKAI UNIVERSITY

Chairman Tetsuo TAKAHASHI
Members Ichiro NAKAGAWA Masakazu SUZUKI
Kazuyoshi TSUCHIYA Hiroyuki MORIYAMA
Masao ISOMURA Hisao KIKUGAWA
Takashi ASAKA

The School of Engineering of Tokai University publishes two kinds of Reports: the report written in English (once a year) and the one written in Japanese (once a year).

*

*

*

Any requests for this proceedings should be addressed to the Editorial Committee of Proceedings of the School of Engineering Tokai University, 4-1-1, Kitakaname, Hiratsuka-shi, Kanagawa-ken. Japan

September 30, 2022

Attention:

The name of this PROCEEDINGS has been changed from 2018 edition as follows.

「PROCEEDINGS OF *THE SCHOOL OF ENGINEERINGS*」